ISPRS Journal of Photogrammetry and Remote Sensing 190 (2022) 301–321

Contents lists available at ScienceDirect

ISPRS Journal of Photogrammetry and Remote Sensing

journal homepage: www.elsevier.com/locate/isprsjprs

Georeferencing oblique PhenoCam imagery

Youssef O Kaddoura [a,c,*], Benjamin Wilkinson [a,b], Trina Merrick [d], Grenville Barnes [a], Katharyn Duffy [e], Eben Broadbent [a,c], Amr Abd-Elrahman [a,b], Michael Binford [g], Andrew D Richardson [e,f]

[a] Geomatics Program, School of Forest, Fisheries, and Geomatics Sciences, University of Florida, Gainesville, FL 32611, USA
[b] Geospatial Mapping & Application (GMAP) Laboratory, University of Florida, Gainesville, FL 32611, USA
[c] Spatial Ecology & Conservation (SPEC) Lab, University of Florida, Gainesville, FL 32611, USA
[d] Remote Sensing Division, Naval Research Laboratory, Washington 20375, USA
[e] School of Informatics, Computing & Cyber Systems, Northern Arizona University, Flagstaff, AZ 86011, USA
[f] Center for Ecosystem Science and Society, Northern Arizona University, Flagstaff AZ 86011, USA
[g] Department of Geography, University of Florida, FL 32611, USA

ARTICLE INFO

Keywords:
Photogrammetry
Oblique Imagery
Near-surface Remote-Sensing
Georeferencing

ABSTRACT

The high temporal and spatial resolution of ecosystem data captured by tower-mounted PhenoCams have established these instruments as fundamental tools in phenological studies and positioned them as a critical mid-step between airborne or spaceborne and *in-situ* data in ecological research. However, adding spatial precision can further expand PhenoCam network applications and attract more users, such as drawing more phenological scientists to the near-surface remote sensing research field. In this study, a georeferencing approach was established to enhance research infrastructure for PhenoCams. Advanced photogrammetric techniques were applied to the camera field of view to geo-enable all pixels, tying them to their location on Earth and adding more usable information to datasets in addition to the current "region of interest" (ROI) level data. The georeferencing method is presented along with the photogrammetric equations that enable going from object space coordinates (3D) to image space coordinates (2D). This method was tested and demonstrated on PhenoCam data at Ordway Swisher Biological Station (OSBS), located in Melrose, Florida, USA. Statistical and sensitivity analyses show that projected pixel-location can be as accurate as 1.5 pixels RMSE for the presented case study, corresponding to object space accuracy of 10 cm, 20 cm, and 30 cm at distances of 100 m, 200 m, and 300 m, respectively. In addition, geo-located PhenoCam data at OSBS was co-located with Moderate Imaging Spectrometer (MODIS) data and characterized. These results demonstrate that the techniques presented reliably provide additional data from PhenoCams that are useful for ecosystem-level studies. By providing each pixel's absolute location corresponding to its place in the real world efficiently, this research introduces a higher degree of spatial precision to every phenological observation from the PhenoCam at OSBS. This presentation of reproducible steps and analysis facilitates implementation for other PhenoCam data as well as other obliquely mounted cameras.

1. Introduction

Terrestrial cameras on stationary platforms have increased in number and improved technologically over the last decades, providing a rich source of Earth Observation data by recording rapid, repeated images, or even video. (Crowson, Birkemeier, Klein, & Miller, 1988; R. Holman, Sallenger, Lippmann, & Haines, 1993; R. A. Holman & Stanley, 2007; R. A. Holman, Symonds, Thornton, & Ranasinghe, 2006; Richardson et al., 2018; Richardson et al., 2007b; Sonnentag et al., 2012; Stilwell & Pilon, 1974; Stockdon & Holman, 2000). For example, two successful stationary camera programs, the Argus and PhenoCam Networks' cameras, have been adopted worldwide (Crowson et al., 1988; Richardson et al., 2018; Richardson et al., 2007b). Efforts to georeference images in these networks broadly establishied photogrammetric methods that allow linking image space to object space. (Andriolo, Sanchez-Garcia, & Taborda, 2019; Conlin et al., 2020; Holland & Holman, 1997b; Holland, Holman, Lippmann, Stanley, & Plant, 1997a; Sanchez-Garcia, Balaguer-Beser, & Pardo-Pascual, 2017).

* Corresponding author.
E-mail address: Kaddoura@ufl.edu (Y.O. Kaddoura).

https://doi.org/10.1016/j.isprsjprs.2022.05.012
Received 13 December 2021; Received in revised form 24 May 2022; Accepted 27 May 2022
Available online 11 July 2022

Fig. 1. Canopy sizes that corresponds to the four ROIs.

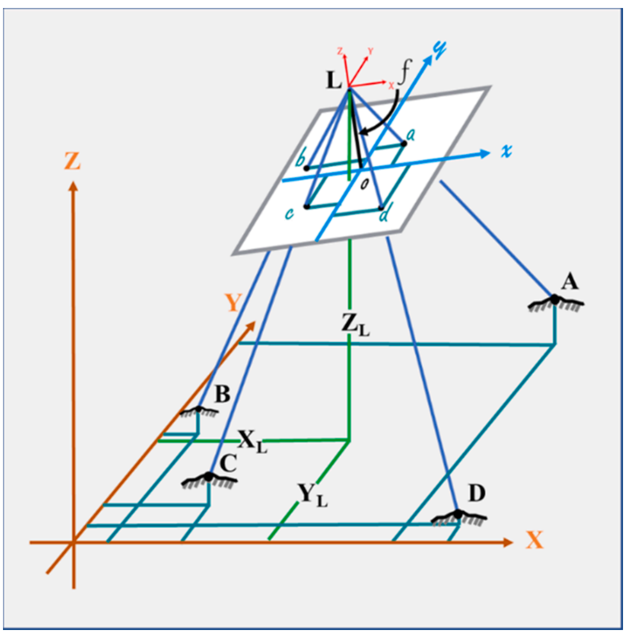

Fig. 2. Shows PhenoCam coordinate system. A through D corresponds to the four ground control points.

PhenoCams are tower-mounted network-enabled digital cameras deployed at National Ecological Observatory Network (NEON) sites and other locations around the world. They enable automated acquisition of terrestrial remote sensing data from multichannel imaging sensors to observe ecosystems of interest (Richardson, 2007a; Richardson et al., 2018; schwartz, 2013).

Previous research work that covers preprocessing methods for PhenoCam is done using a modeling framework called PhenoR which captures ROI (non-georeferenced) PhenoCam imagery and combined it with three other common phenology datasets (Hufkens et al., 2012). PhenoCam data have been used extensively to analyze, compare, and evaluate phenological findings from satellite-based sensors (Richardson et al., 2018).

PhenoCams are mounted at oblique angles on the towers, and regions of interest (ROIs) within the PhenoCam fields of view are identified, established, and tracked to represent ecosystem function, structure, and phenology. This current PhenoCam approach to characterizing phenological features, therefore, is geospatially limited to the ROIs selected at each site. The ROIs are coarsely georeferenced based on tertiary information at the tower site. An example of ROI selection corresponding to four different pine tree canopies at Ordway Swisher Biological Station, Melrose, FL, with a size range of 12 to 20 m^2, is shown in Fig. 1. While tracking ROIs has resulted in greater understanding of ecosystem function, structure, and phenology, there is opportunity for improvement.

The applicability and effectiveness of PhenoCam data could be further increased by systematically co-locating these obliquely mounted optical camera data to ground coordinates for expanded data usage and applications.First, a large amount of data exists outside of ROIs collected by PhenoCams that is excluded from analyses and no method can easiy integrate this information into studies. Second, reducing uncertainty in ROI locations would improve integration into studies. Third, accurate geolocation of both instantaneous field of view (IFOV) that is binned into predefined grid cell/parallelogram from remote sensing data and ROIs imagery data would facilitate precisely matching these data to other data sources, such as satellite measurements.This study establishes an automated process to georeference PhenoCam pixels to a well-defined coordinate system for co-location with data from other remote sensing sources and decreases uncertainties when integrating these data into studies. The objectives were to increase the useable data obtained from PhenoCam sensors and improve fusion and scalability with other data types by georeferencing all pixels within PhenoCam images. Specifically, this is accomplished by 1) Georeferencing PhenoCam images to the pixel level instead of ROI level, 2) Performing sensitivity analysis and reliability testing for the georeferenced PhenoCam pixels, and 3) Creating a generalized framework for accurately georeferencing all PhenoCam imagery.

2. Methods

2.1. Georeferencing model

The photogrammetric technique presented here encompasses two main tasks: space resection to determine interior and exterior orientation parameters (IOPs, EOPs) and back-projection to enable transferring 3D object space coordinates to 2D image coordinates.

Space resection allows estimation of a camera's EOPs, (X_L,Y_L,Z_L) and (ω, φ, κ), the positional and angular orientation of the camera in a global coordinate system when a photo was taken, respectively. In this method, EOPs are assumed to be fixed once established via space resection for PhenoCams. In addition to the EOPs, focal length, f, which is a major component of the IOPs is also resolved in the presented space resection procedure. Fig. 2 shows the image space coordinate system centered at the exposure station L, as well as the object space coordinate system in orange. Both are treated as independent coordinate systems that are related by applying the collinearity equations. As per Fig. 3, the collinearity equations represent the ideal situation in that the object, the lens (the rear nodal point of the camera), and the image all lie along a

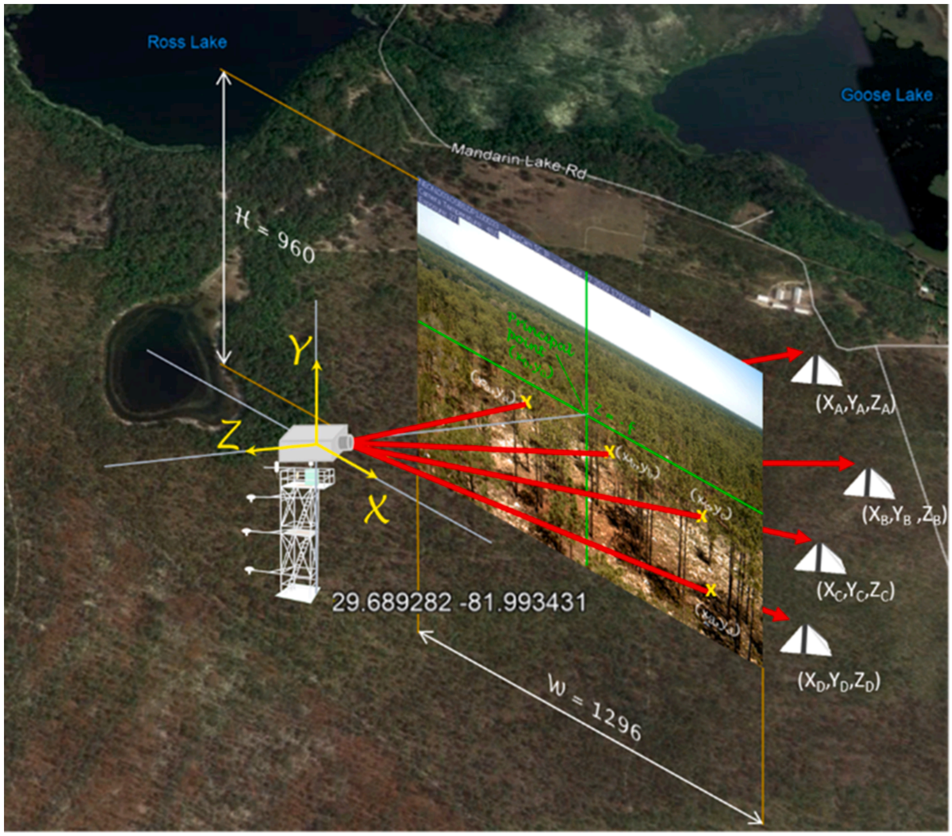

Fig. 3. Shows a diagram of space resection by collinearity method.

straight line (Wolf, Dewitt, & Wilkinson, 2014).

Two collinearity equations can be written for each observed point. For example, the collinearity equations for some point A are:

$$x_a = x_o - f\left[\frac{m_{11}(X_A - X_L) + m_{12}(Y_A - Y_L) + m_{13}(Z_A - Z_L)}{m_{31}(X_A - X_L) + m_{32}(Y_A - Y_L) + m_{33}(Z_A - Z_L)}\right] \quad (1)$$

$$y_a = y_o - f\left[\frac{m_{21}(X_A - X_L) + m_{22}(Y_A - Y_L) + m_{23}(Z_A - Z_L)}{m_{31}(X_A - X_L) + m_{32}(Y_A - Y_L) + m_{33}(Z_A - Z_L)}\right]$$

Where the Rotation Matrix (M) is formed as shown below:

$$M = \begin{bmatrix} m_{11} & m_{12} & m_{13} \\ m_{21} & m_{22} & m_{23} \\ m_{31} & m_{32} & m_{33} \end{bmatrix} \quad (2)$$

And.

$$m_{11} = \cos(\varphi)\cos(\kappa)$$

$$m_{12} = \sin(\omega)\sin(\varphi)\cos(\kappa) + \cos(\omega)\sin(\kappa)$$

$$m_{13} = -\cos(\omega)\sin(\varphi)\cos(\kappa) + \sin(\omega)\sin(\kappa)$$

$$m_{21} = -\cos(\varphi)sin(\kappa)$$

$$m_{22} = -\sin(\omega)\sin(\varphi)\sin(\kappa) + \cos(\omega)\cos(\kappa)$$

$$m_{23} = \cos(\omega)\sin(\varphi)\sin(\kappa) + \sin(\omega)\cos(\kappa)$$

$$m_{31} = \sin(\varphi)$$

$$m_{32} = -\sin(\omega)\cos(\varphi)$$

$$m_{33} = \cos(\omega)\cos(\varphi) \quad (3)$$

Where,

- $f$is the focal length (principle distance).
- $x_a$and $y_a$are the coordinate measurements of the image point in the camera coordinate system.
- $x_0$and y_0 are the coordinates of the principal point
- (X_L,Y_L,Z_L) and (ω,φ,κ), the positional and angular orientation of the camera in a global coordinate system
- (X_A,Y_A,Z_A) are the 3D coordinates of an object point.

In the conventional approach, a minimum of three GCPs is needed to compute the six EOPs, but since the f is considered an unknown, a minimum of four points is needed here. However, using unified least-squares allows a decrease in the total number of observations needed as it mitigates the degeneracy caused by having fewer fundamental observations than unknowns.

The unified least squares approach (Mikhail & Ackermann, 1982) allows the simple inclusion of direct observations of the unknowns with rigorous adjustment weighting based on estimated observation uncertainty. This method also readily allows estimation of precision for the unknown parameters, and propagation of uncertainty to subsequent object-to-image space transformations.

Initializing the unknowns is an essential part of the unified least-squares space resection approach. The angular orientation definitions of the camera are defined as ω: rotation about the X axis; φ: rotation about the once-rotated Y axis; and κ: rotation about the twice-rotated Z axis. These angles can be approximated by leveraging the fact that PhenoCams are mounted so that they point roughly north, images are leveled relative to the horizon, and that the tilt from vertical can be visually approximated by inspecting the imagery. Approximations of (X_L,Y_L,Z_L) may be found in many ways, including ground-based methods using GNSS or a total station or by aerial remote sensing data. For example, in this study, airborne LIDAR was used to estimate these parameters. f may be approximated using the manufacturer's specifications. Corrections, comprising Δ, are solved and added to current

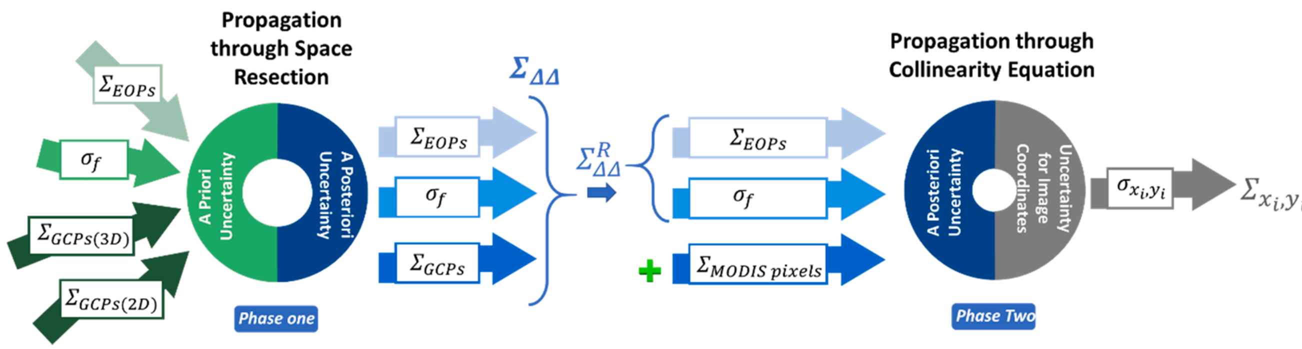

Fig. 4. Shows the propagated updated positions and uncertainty of object space points.

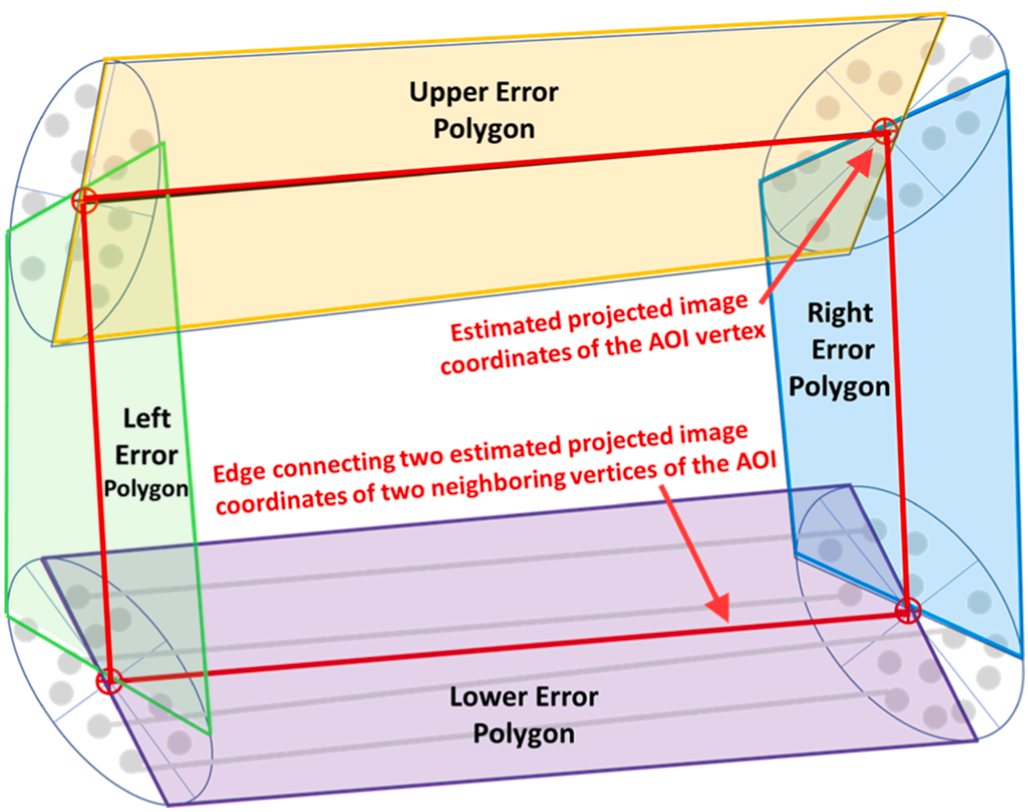

Fig. C1. Diagram of the convergence of four error polygons corresponding to the four edges of an area of interest. The red line joining the central red dots represents the edge connecting two computed image coordinates in all parts of the figure. (For interpretation of the references to colour in this figure legend, the reader is referred to the web version of this article.)

approximations of the unknowns iteratively, repeating the solution using Eqn. (4) until convergence of Eqn. (5), the standard deviation of unit weight.

$$\Delta = \left(B^T WB + \dot{W}\right)^{-1}\left(B^T W\varepsilon + \dot{W}C\right) \tag{4}$$

$$S_0 = \sqrt{\frac{\varepsilon^T W\varepsilon + C^T\dot{W}C}{n.o.}} \tag{5}$$

In Eqn. (4), the weight matrix associated with the uncertainty of direct observations of the unknown parameters is represented by $\dot{W}$, where C contains their computed values at the current iteration subtracted from their directly measured values. The weight matrix associated with the uncertainty of image point observations, represented by W, is equal to the inverse of the image point observation covariance matrix. The vector containing all measured image coordinates minus all computed image coordinates based on the current iteration's approximation of unknowns is represented by ε. Appendix A shows that the covariance values on the off-diagonal of W and $\dot{W}$ are zeros implying that there is no correlation between measurements, a reasonable assumption. The Jacobian matrix, B, contains partial derivatives of the collinearity equations with respect to all the parameters. See Appendix A for detailed matrix definitions.

The focal length was initialized to 1500 PhenoCam pixels based on the manufacturer's specifications of 6.2 mm as the focal length and image dimension of 5.76 × 4.29 mm, the image dimensions (length, width) in pixels, the positional coordinates of the lens X_L, Y_L, Z_L in meters (all in UTM coordinates – zone 17) and derived by 2016 LiDAR dataset captured by NEON's AOP, and the angular attitude of the lens ω, φ, and κ in degrees, and were initially set to were set to 50°, −2°, and 0° respectively. The Ground Control Points (GCPs) list the GCP number, the image space (2D) coordinates (x_i, y_i), measured in PhenoCam pixels

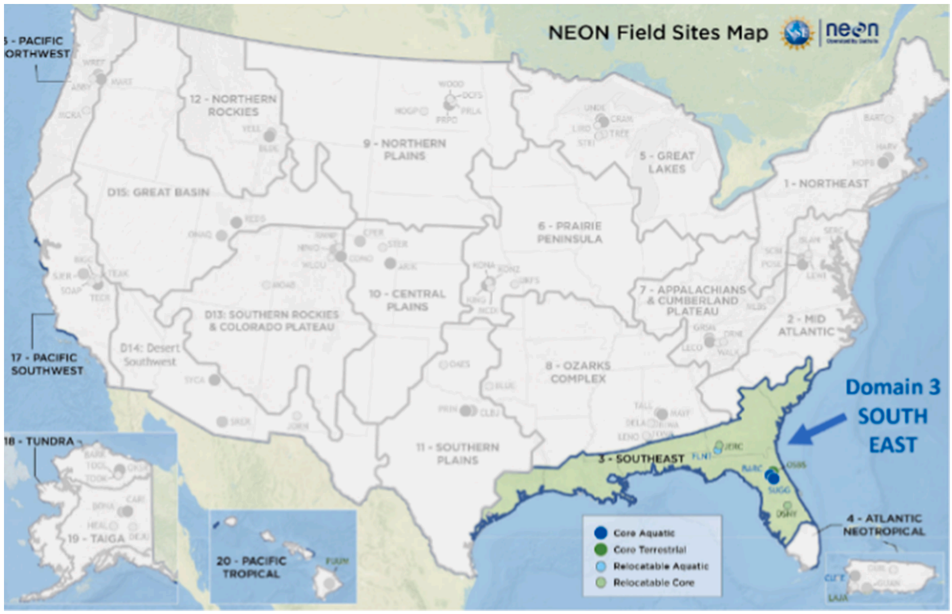

Fig. 5. NEON Ecoclimatic Domain map. Domain 3 is highlighted and indicating the location of OSBS (Battelle, 2020).

Fig. 6. GCP placement at OSBS. The targets can be seen as white pyramids in the right panel. A) PhenoCam images showing planned, and B) showing actual.

Table 1
Four PhenoSynth/MODIS pixels/grid cells that corresponds to 9 vertices (A, B, C, D, E, F, G, H, and I in Fig. 7) (Morisette et al., 2021).

PhenoSynth / MODIS	Corresponding Vertices
42_43	A,B,D, and E
42_44	B,C,E, and F
43_43	D,E,G, and H
43_44	E,F,H, and I

using AutoCad, and their corresponding PhenoCam pixel uncertainties $(\sigma_{x_i}, \sigma_{y_i})$, the object space (3D) coordinates of all GCPs (X_O, Y_O, Z_O) measured using RTK GNSS in meters (all in UTM coordinates) along with their uncertainties $(\sigma_{X_O}, \sigma_{Y_O}, \sigma_{Z_O})$, determined by the typical RTK GNSS horizontal accuracy of 2 cm and vertical accuracy of 4 cm.

Once the space resection solution has converged, the resulting values for f,ω, φ, κ, X_L,Y_L,Z_L may be applied using the collinearity equations (Eqn. (1)) to transform any object space point coordinates (X_i,Y_i,Z_i) to their corresponding image space coordinates (x_i,y_i). Thus, any georeferenced 3D geospatial data may be projected onto the PhenoCam imagery, and a direct comparison of that data to PhenoCam imagery may be made.

In addition to the computation of image coordinates (x_i,y_i) from input variables (ground coordinates, EOPs, f), the collinearity equations allow propagation of input variable uncertainties to the resulting/output image coordinate uncertainties $(\sigma_{x_i}, \sigma_{y_i})$. Fig. 4 illustrates the uncertainty propagation, which has two phases. Phase one corresponds to the uncertainty estimation of the resolved GCP coordinates, EOPs, and f. Phase two corresponds to the propagation of the uncertainties from phase one and uncertainties in arbitrary ground coordinates, such as remote sensing data bounding-polygon vertices, to uncertainties in projected image space coordinates.

These are established using Jacobian matrix B (see Appendix A) of the converged solution. The resulting equation of the Phase 1 propagated error is:

$$\Sigma_{\Delta\Delta} = \begin{bmatrix} \sigma_f^2 & \Sigma_{f,EOPs} & \Sigma_{f,GCPs} \\ \Sigma_{EOPs,f} & \Sigma_{EOPs} & \Sigma_{EOPs,GCPs} \\ \Sigma_{GCPs,f} & \Sigma_{GCPs,EOPs} & \Sigma_{GCPs} \end{bmatrix} = s_0^2\left(B^T WB + \dot{W}\right)^{-1} \tag{6}$$

where $\Sigma_{\Delta\Delta}$ is the *a posteriori* covariance matrix of all the unknowns, σ_f^2, Σ_{EOPs}, Σ_{GCPs} are the variance and covariance matrices of the solved focal length, EOPs, and GCPs, respectively, and $\Sigma_{i,j}$ are the cross-covariance sub-blocks between parameter sets $i$and j.

Phase 2 corresponds to generating the covariance matrix shown in Eqn. (7), which enables establishing error ellipses corresponding to each

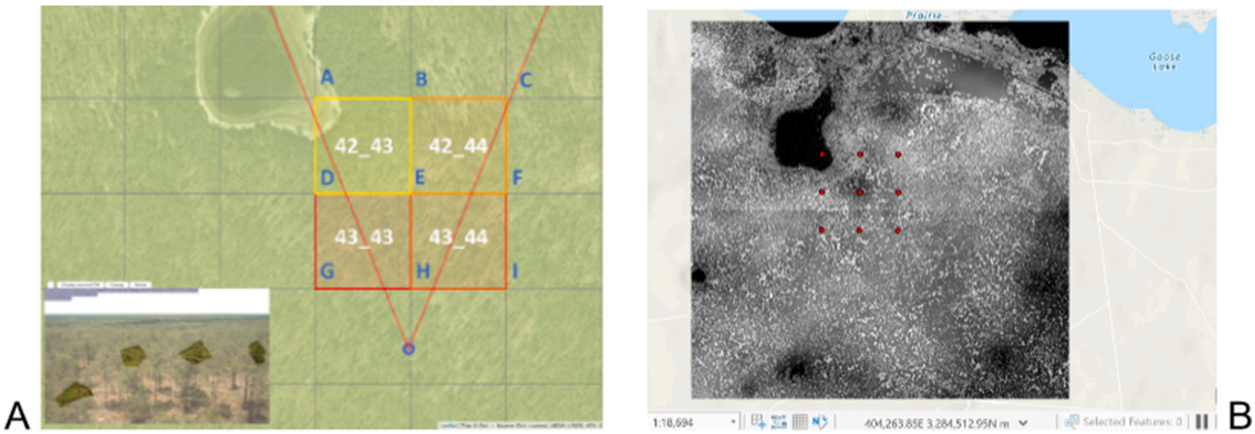

Fig. 7. Showing four PhenoSynth pixels/grid cells that overlap with PhenoCam field of view. A) showing screenshot of PhenoSynth application, and B) showing the LIDAR-derived raster mapped at the OSBS site with the vertices of PhenoSynth pixels/grid cells indicated.

Table 2
Space resection input values of initial approximations and observations and their corresponding labels. The Camera Parameters shows the camera focal length in PhenoCam pixels, the positional coordinates of the lens X_L, Y_L, Z_L in meters, and the angular attitude of the lens ω, φ, and κ in degrees, The Ground Control Points (GCPs) list the GCP number, the image space (2D) coordinates (x_i,y_i), and their corresponding PhenoCam pixel uncertainties (σ_{x_i},σ_{y_i}), the object space (3D) coordinates of all GCPs (X_O, Y_O,Z_O) measured in meters along with their uncertainties (σ_{X_O},σ_{Y_O},σ_{Z_O}).

Camera Parameters	**f (pixel)**										
	1500										
	length (pixel)					**width (pixel)**					
	1296					960					
	X_L (m)			**Y_L (m)**				**Z_L (m)**			
	403885.73			3284770.66				51.46			
	ω (°)			**φ (°)**				**κ (°)**			
	50			−2				0			
Ground Control Points (GCPs)	**GCP #**	**x_i (pixel)**	**y_i (pixel)**	**σ_{xi} (pixel)**	**σ_{yi} (pixel)**	**X_O (m)**	**Y_O (m)**	**Z_O (m)**	**σ_{XO} (m)**	**σ_{YO} (m)**	**σ_{ZO} (m)**
	1	34	80	1	1	403858.95	3284836.23	18.36	0.02	0.02	0.04
	2	372	85	1	1	403875.36	3284835.55	18.78	0.02	0.02	0.04
	3	649	94	1	1	403888.66	3284835.62	19.08	0.02	0.02	0.04
	4	859	73	1	1	403898.33	3284833.06	19.24	0.02	0.02	0.04
	5	1084	51	1	1	403908.01	3284830.46	19.34	0.02	0.02	0.04
	6	1096	226	1	1	403915.34	3284851.15	19.60	0.02	0.02	0.04
	7	888	225	1	1	403903.23	3284851.61	19.44	0.02	0.02	0.04
	8	646	232	1	1	403889.07	3284853.81	19.17	0.02	0.02	0.04
	9	348	211	1	1	403871.44	3284852.08	18.70	0.02	0.02	0.04
	10	91	209	1	1	403856.09	3284852.85	18.37	0.02	0.02	0.04
	11	74	319	1	1	403847.35	3284874.85	18.24	0.02	0.02	0.04
	12	322	312	1	1	403866.28	3284871.67	18.61	0.02	0.02	0.04
	13	629	360	1	1	403888.48	3284882.03	19.11	0.02	0.02	0.04
	14	903	366	1	1	403910.03	3284881.29	19.53	0.02	0.02	0.04
	15	1076	384	1	1	403924.82	3284884.95	19.83	0.02	0.02	0.04
	15a	1192	277	1	1	403924.12	3284858.97	19.79	0.02	0.02	0.04
	16	1093	432	1	1	403931.76	3284901.66	19.78	0.02	0.02	0.04
	17	726	418	1	1	403897.56	3284899.91	19.26	0.02	0.02	0.04
	18	593	431	1	1	403886.44	3284904.97	19.03	0.02	0.02	0.04
	19	398	427	1	1	403867.04	3284906.57	18.69	0.02	0.02	0.04
	19a	254	421	1	1	403853.52	3284905.51	18.48	0.02	0.02	0.04
	20	234	491	1	1	403842.44	3284943.13	18.12	0.02	0.02	0.04

Table 3
Converged solution of space resection for EOP and IOP and their corresponding labels.

f (pixel)			**σ_f (pixel)**		
1475.08			3.31		
XL (m)	**YL (m)**	**ZL (m)**	**σ_{XL} (m)**	**σ_{YL} (m)**	**σ_{ZL} (m)**
403886.64	3284769.73	51.37	0.06	0.19	0.09
ω (°)	**φ (°)**	**κ (°)**	**σ_ω (°)**	**σ_φ (°)**	**σ_κ (°)**
78.55	−1.61	−0.29	0.04	0.03	0.04

computed image space coordinate result as shown in Fig. 4. Jacobian matrix A contains partial derivatives of the collinearity equations with respect to all the space-resection resolved parameters and the ground coordinates that are projected. The parameters listed in Eqn. (7) correspond to the focal length f, object space coordinates of the lens (X_L,Y_L,Z_L) plus its angular attitude (ω, φ, κ), and the ground space coordinates ($X_1, Y_1, Z_1, X_2, Y_2, Z_2, \ldots\ldots, X_m, Y_m, Z_m$), where m is the number of ground space points that are projected. Note that Σ_{MODIS_P} is the covariance matrix associated with the estimated ground space coordinate errors.

Table 4
The standard deviation of each computed MODIS vertex.

MODIS Vertex	Computed Coordinates		Standard		95% Confidence	
	x (pixel)	y (pixel)	σ_x (pixel)	σ_y (pixel)	σ_x (pixel)	σ_y (pixel)
A	47.49	706.56	3.29	1.77	8.05	4.33
B	619.14	773.36	2.91	1.78	7.12	4.36
C	1187.68	783.30	3.31	1.85	8.10	4.53
D	−302.43	678.58	5.67	2.55	13.87	6.24
E	623.82	707.16	4.58	2.47	11.22	6.04
F	1530.59	713.16	5.53	2.54	13.54	6.23
G	−1760.42	501.90	22.74	6.59	55.67	16.13
H	652.03	620.45	11.73	6.09	28.71	14.91
I	2880.44	509.32	20.44	6.30	50.05	15.42
Mean			8.91	3.55	21.81	8.69

$$\Sigma_{xy} = A\Sigma^{R}_{\Delta\Delta}A^{T}$$

$$\Sigma_{xy} = \begin{bmatrix} \sigma^2_{x_i} & \sigma_{x_i}\sigma_{y_i} \\ \sigma_{y_i}\sigma_{x_i} & \sigma^2_{y_i} \end{bmatrix}$$

$$\Sigma^{R}_{\Delta\Delta} = \begin{bmatrix} \sigma^2_f & 0 & 0 \\ 0 & \Sigma_{EOPs} & 0 \\ 0 & 0 & \Sigma_{MODIS_P} \end{bmatrix}$$

$$\Sigma^{R}_{\Delta\Delta} = \begin{bmatrix} \sigma^2_f & 0 & 0 \\ 0 & \Sigma_{EOPs} & 0 \\ 0 & 0 & \Sigma_{MODIS_P} \end{bmatrix}$$

$$\Sigma_{EOPs} = \begin{bmatrix} \sigma^2_{X_L} & \sigma_{X_L}\sigma_{Y_L} & \sigma_{X_L}\sigma_{Z_L} & \sigma_{X_L}\sigma_{\omega} & \sigma_{X_L}\sigma_{\varphi} & \sigma_{X_L}\sigma_{\kappa} \\ \sigma_{Y_L}\sigma_{X_L} & \sigma^2_{Y_L} & \sigma_{Y_L}\sigma_{Z_L} & \sigma_{Y_L}\sigma_{\omega} & \sigma_{Y_L}\sigma_{\varphi} & \sigma_{Y_L}\sigma_{\kappa} \\ \sigma_{Z_L}\sigma_{X_L} & \sigma_{Z_L}\sigma_{Y_L} & \sigma^2_{Z_L} & \sigma_{Z_L}\sigma_{\omega} & \sigma_{Z_L}\sigma_{\varphi} & \sigma_{Z_L}\sigma_{\kappa} \\ \sigma_{\omega}\sigma_{X_L} & \sigma_{\omega}\sigma_{Y_L} & \sigma_{\omega}\sigma_{Z_L} & \sigma^2_{\omega} & \sigma_{\omega}\sigma_{\varphi} & \sigma_{\omega}\sigma_{\kappa} \\ \sigma_{\varphi}\sigma_{X_L} & \sigma_{\varphi}\sigma_{Y_L} & \sigma_{\varphi}\sigma_{Z_L} & \sigma_{\varphi}\sigma_{\omega} & \sigma^2_{\varphi} & \sigma_{\varphi}\sigma_{\kappa} \\ \sigma_{\kappa}\sigma_{X_L} & \sigma_{\kappa}\sigma_{Y_L} & \sigma_{\kappa}\sigma_{Z_L} & \sigma_{\kappa}\sigma_{\omega} & \sigma_{\kappa}\sigma_{\varphi} & \sigma^2_{\kappa} \end{bmatrix} \quad (7)$$

Error ellipses allow a graphical depiction of the uncertainty regions of the projected image space coordinates. The calculated standard deviations σ_{x_i} and σ_{y_i} are parallel to the base and side of the error rectangle, and the calculated semimajor and semiminor axes of the rotated error

Table 5
Showing the standard error of unit weight for each iteration.

Iteration #	0	1	2	3	4	5
S_0	545.193	43.013	2.187	0.970	0.969	0.969

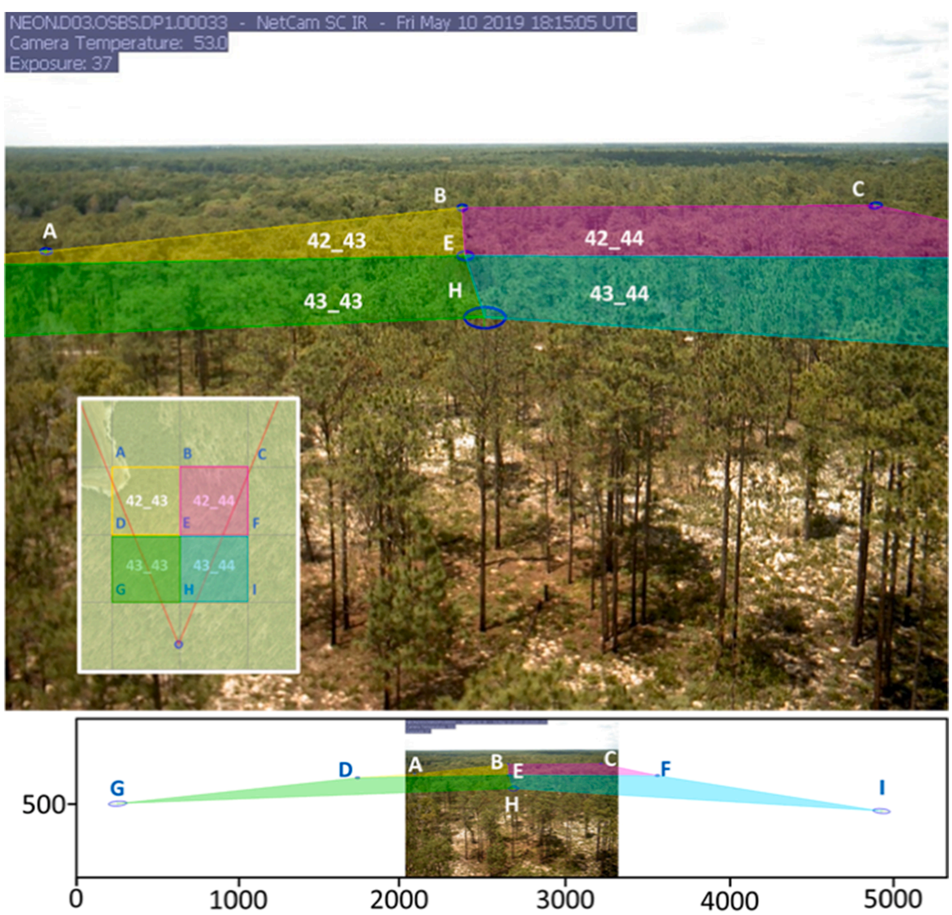

Fig. 8. PhenoCam image at OSBS with polygons overlaid from the PhenoSynth application representing the corresponding PhenoSynth/MODIS pixels/grid cells (top). The inset represents a nadir view of the four pixels/grid cells (top). The PhenoCam image with the full extent of PhenoSynth/MODIS pixels/grid cells overlaid (bottom). The vertices are represented by A, B, C, D, E, F, G, H, I, and PhenoSynth pixel/grid cell IDs are represented by 42_43, 43_43, 42_44, 43_44.

Table 6
Validation example standard deviation vs. RMSE.

Check	Image Space Coordinates								
	Truth Values (pixel)		Computed Values (pixel)		Propagated Uncertainty (pixel)		Coordinates Differences (pixel)		2D Distance Difference (pixel)
	x	y	x	y	x	y	x	y	
2	372	85	371.05	86.11	0.72	0.78	−0.95	1.11	1.46
4	859	73	858.59	71.64	0.71	0.81	−0.41	−1.36	1.42
7	888	225	886.92	224.35	0.44	0.56	−1.08	−0.65	1.26
9	348	211	347.49	210.49	0.45	0.57	−0.51	−0.51	0.72
12	322	312	320.41	311.37	0.45	0.55	−1.59	−0.63	1.71
14	903	366	902.21	366.15	0.50	0.59	−0.79	0.15	0.80
15	1076	384	1076.49	385.06	0.69	0.69	0.49	1.06	1.17
17	726	418	725.15	417.81	0.47	0.64	−0.85	−0.19	0.87
19	398	427	395.65	426.76	0.59	0.69	−2.35	−0.24	2.36
20	234	491	233.49	488.76	0.99	0.93	−0.51	−2.24	2.30
						Mean	0.86	0.35	1.41
						Std. Dev.	0.71	0.96	
						RMSE	1.11	1.02	

ellipse are represented by S_u, S_v respectively, with an α being the clockwise angle between major axis U and the image space negative y-axis. The outer (95% confidence region) and inner (standard ellipse, 39.347% confidence region) error ellipses. The semimajor and semi-minor axes corresponding to direction and magnitude of the largest and smallest value of the positional uncertainty of any specific point, respectively (Gerald, 1987). The 95% error ellipse has a rotated semi-major axis with length equal to 2.45 times that of the standard semi-major axis S_u and a rotated semiminor axis with length equal to 2.45 times the standard semiminor axis S_v. For functions of one dimension, 95.45% and two standard deviations are widely accepted (Burt, Barber, & Rigby, 2009). However, this is not the case here because the space is two-dimensional. Under the assumption that the center of the ellipse is located at the estimated projected image coordinates, then there is a 95% probability that the true image coordinates are anywhere within the outer error ellipse. The computed PhenoCam image location of a 3D position, such as a vertex of a georeferenced satellite image pixel/grid cell, would be at the center of the ellipse.

The larger the ellipse, the less accurate and the higher the inexactness of the estimated position. The error ellipse parameters are computed as outlined in (Ghilani, 2017):

$$tan2\alpha = \frac{2\sigma_{xy}}{\sigma_y^2 - \sigma_x^2}$$

$$semi-majoraxis = S_u = \sqrt{\sigma_x^2 \times sin^2\alpha + 2 \times \sigma_{xy} \times cos\alpha \times sin\alpha + \sigma_y^2 \times cos^2\alpha} \quad (8)$$

Connecting two centers of error ellipses provides the computed edge of the AOI. The error polygon method approximates the uncertainty impact of the two neighboring vertices on the location of each edge/side of an area of interest (AOI). A diagram of the uncertainty regions for the edges of an AOI is shown in Fig. C-1. The area inside the error polygon is established by connecting the tangency points for the error ellipsis of the AOI vertices that are used to draw an edge of the AOI. Connecting two 95% error ellipses provides an illustration of approximate bounds on the true projected edge locations Fig. C-1.

Generating the correlation matrix for the converged solution parameters allows a better understanding of the relationship among parameters and strength of parameter resolution. $\rho_{ij=}\sigma_{ij}^2/\sigma_i\sigma_j$was followed to compute each correlation coefficient between each pair [i,j] of the considered variables (f,ω, φ, K, X_L,Y_L,Z_L) accordingly (Burt et al., 2009).

3. Materials

3.1. Study area

Measurements, testing, and ground-truthing for the study were carried out at Ordway Swisher Biological Station (OSBS) in Melrose, FL. OSBS is a NEON site (tower location: 29.689282°N, −81.993431°W), and a research, teaching, and extension facility of the University of Florida. (Fig. 5). Overall, the southeast domain is considered a warm, wet climate that supports subtropical forest conditions.

On April 11th, 2019, fieldwork was conducted at OSBS to collect measurements of ground control points (GCPs). GCP locations were established within 180 m of the tower within the field of view (FOV) of the PhenoCam. Notably, vegetation is sparse around the tower in OSBS, allowing for the use of individual multimodal (LIDAR and imagery) pyramid targets as GCP's see Fig. 6 (Wilkinson et al., 2019). Fig. 6 illustrates planned vs. actual locations of the identified GCPs (n = 22 close-range GCPs), which are spatially distributed such that they cover the lower half of the image. Determining the accurate and precise location information for the targets was accomplished through real-time kinematic (RTK) global navigation satellite system (GNSS) survey, according to the methods in (Johnson et al., 2021). All 22 GCPs were surveyed, ensuring a fixed integer solution, thus providing accuracy on the order of 2 cm.

3.2. Study area data

Using the method described in Section "Space Resection by Collinearity", initial values for the OSBS PhenoCam for ω, φ, and κ were set to 50°, −2°, and 0°, respectively. Focal length, f, was initialized to 1500 PhenoCam pixels based on the manufacturer's specifications of 6.2 mm as the focal length and image dimension of 5.76 × 4.29 mm. The approximation of the 3D coordinates of the OSBS PhenoCam, X, Y_L,Z_L, was achieved by using the 2016 LiDAR dataset captured by NEON's AOP (CloudCompare, 2020).

The four MODIS/PhenoSynth pixels/grid cells that overlap the most with the PhenoCam field of view were identified, and the metadata files for those individual pixels/grid cells were downloaded.

The vertical coordinates for the 9 vertices in Table 1 were determined via the Digital Surface Model (DSM) derived from NEON's AOP LIDAR and the horizontal coordinates of the vertices in ArcGIS Pro as shown in Fig. 7 (B).

Table 7
Comparison of resulting image coordinates based on different options for sub-meter positional accuracy of the targets.

Check Point No.	Original				Error Standard Deviation (m)															
	0				0.48				0.98				1.48				1.98			
	x	y	σx	σy	x	y	σx	σy	x	y	σx	σy	x	y	σx	σy	x	y	σx	σy
2	372.95	83.89	0.81	0.91	374.29	86.32	4.09	6.62	368.51	83.43	5.38	8.77	389.56	54.42	12.23	18.91	379.96	80.70	15.51	24.18
4	859.41	74.36	0.81	0.94	868.05	83.98	4.16	6.97	860.33	65.31	5.57	8.96	879.02	41.36	12.76	19.71	868.02	70.65	15.91	24.67
7	889.08	225.65	0.53	0.68	895.43	233.87	2.63	4.67	884.57	217.42	3.88	6.80	902.05	197.04	9.39	16.27	892.58	220.81	12.16	21.53
9	349.46	211.51	0.55	0.68	349.40	212.01	2.73	4.67	341.08	213.54	3.97	6.95	362.13	186.40	9.35	16.02	353.92	207.77	12.44	21.71
12	323.59	312.63	0.51	0.63	322.43	311.11	2.28	4.19	312.08	316.42	3.61	6.61	333.28	290.36	8.47	15.52	326.18	307.84	11.77	21.59
14	903.79	365.85	0.54	0.65	907.76	371.79	2.30	4.40	893.99	357.82	3.49	6.63	910.37	340.24	8.42	15.82	902.37	358.79	11.34	21.32
15	1075.51	382.94	0.72	0.74	1080.78	391.03	3.06	5.37	1064.16	371.27	4.53	7.96	1080.20	356.28	10.79	18.93	1071.85	375.08	14.46	25.38
17	726.85	418.19	0.51	0.68	728.33	420.44	2.11	4.57	715.28	414.02	3.12	6.54	732.13	394.84	7.24	14.78	725.19	410.52	9.92	19.79
19	400.35	427.24	0.62	0.73	398.95	424.54	2.50	5.01	386.65	430.30	3.72	7.19	406.64	406.63	8.25	15.92	400.56	420.30	11.53	21.62
20	234.51	493.24	1.00	0.94	231.34	486.55	3.85	6.86	217.04	500.40	5.36	9.41	239.42	474.96	11.44	20.07	234.36	485.34	15.66	26.69
Mean			0.66	0.76			2.97	5.33			4.26	7.58			9.83	17.20			13.07	22.85

4. Results

4.1. Space resection

Space Resection was implemented using the initial approximation and observations mentioned in the input list shown in Table 2, allowing the determination of the spatial position and orientation of the PhenoCam shown in Table 3.

EOPs and IOP were determined by the convergence of the space resection method to a unified least-squares solution and were used to compute the image space coordinates of each of the MODIS vertices Fig. 8. The application of the georeferencing tool was tested by having an input that corresponds to the 3D object space coordinates of the nine vertices (A, B, C, D, E, F, G, H, and I) representing the four MODIS satellite 250 × 250 m pixels/grid cells. 2D coordinates are extracted from PhenoSynth with an uncertainty of 1 m, and vertical coordinates were determined by geoprocessing the NEON's DSM of the site (see Fig. 7) with an uncertainty of 0.5 m. The resulting image coordinates for these vertices (x,y) are established by applying solved PhenoCam parameters using Eqn. (1). Image coordinate estimates are plotted on the PhenoCam image along with the corresponding uncertainty of each vertex.

Note that the warping of PhenoSynth 42_43 is due to elevation variability, where vertex A has an ellipsoidal elevation value (0.39 m) versus the ellipsoidal elevation of vertex B (21.09 m), causing the apparent tilted representation of the polygon Fig. 8. The LIDAR data extracted from NEON's LIDAR point cloud agrees with the survey crew's knowledge and experience for OSBS.

Table 5 shows that the standard error of unit weight converging to a value close to one over six iterations, implying a properly weighted adjustment and proper modeling of observation uncertainties. These results and the lack of apparent outliers indicate that the uncertainty estimates are reliable. The solution converged rapidly in three iterations, with two additional iterations to ensure convergence.

To demonstrate the validity of the work, the surveyed ground points listed in Table 6 were used as independent image truth points, meaning that they were not included in the space resection calculations and only used to check the resulting solution. Space resection was performed using the remaining GCPs (1,3,5,6,8,10,11,13,15a,16,19a) to assess the quality of computed image positions compared to the image truth points. Table 6 provides information on the general image coordinate results and details the residual PhenoCam pixel distance errors for each image truth point. As shown in Table 6, the smallest 2D PhenoCam image space difference was that of checkpoint #9 at 0.72 PhenoCam pixels, and the largest difference was for checkpoint 20 at 2.30 PhenoCam pixels. The mean distance for ground truth to computed points was 1.40 PhenoCam pixels.

Table 6 presents validation point standard deviations and the root-mean-square error (RMSE). In this sample, the standard deviations are 0.71 and 0.96 PhenoCam pixels along the x-axis and y-axis, respectively. The RMSE is 1.11 PhenoCam pixels and 1.02 PhenoCam pixels along the x-axis and y-axis, respectively. The mean of the errors is 0.86 and 0.35 PhenoCam pixels along the x-axis and y-axis, respectively, and being close to zero indicates that there is no systematic error.

4.2. Effect of GCP accuracy

It is anticipated that solution quality may be affected by GNSS accuracy due to, for example, shorter observation sessions (Eckl, Snay, Soler, Cline, & Mader, 2001) and limitations of satellite visibility amidst vegetation canopy. In order to assess the impact of GNSS coordinate quality on the resulting solutions, random errors were added to a subset of GCP coordinates, with the remaining GCPs excluded from the solution and used as checkpoints to evaluate the solutions (see Table B2. Table B3.Table B4.Table B5.). Random, zero-mean errors were applied with varying magnitudes ($\sigma_X = \sigma_Y = [0, 0.48, 0.98, 1.48, 1.98]$, $\sigma_Z = 2\sigma_X$). Table 7 highlights the differences between resulting georeferenced

Table 8
Comparison of resulting image coordinates based on 1000 simulations for each random error magnitude.

Error Standard Deviation	0.48 (m)		0.98 (m)		1.48 (m)		1.98 (m)	
Check Point No.	σ_{dx} (pixel)	σ_{dy} (pixel)	σ_{dx} (pixel)	σ_{dy} (pixel)	σ_{dx} (pixel)	σ_{dy} (pixel)	σ_{dx} (pixel)	σ_{dy} (pixel)
2	4.14	7.06	7.06	11.51	10.00	15.54	13.80	19.97
4	4.42	7.28	7.50	11.38	10.40	15.75	14.02	21.53
7	3.05	5.35	5.84	9.75	8.35	14.66	11.36	20.68
9	2.93	5.37	5.68	10.22	8.42	14.67	11.41	19.35
12	2.60	4.95	5.40	10.04	8.21	14.77	10.75	19.56
14	2.70	5.16	5.46	9.57	7.95	14.68	10.76	20.58
15	3.53	6.21	7.01	11.38	10.12	17.32	13.59	24.26
17	2.37	5.14	4.67	8.96	6.88	13.41	9.20	18.28
19	2.73	5.52	5.30	9.96	7.98	14.43	10.16	18.89
20	4.00	7.27	7.19	12.36	10.66	17.26	13.23	22.08
Mean	3.25	5.93	6.11	10.51	8.90	15.25	11.83	20.52
Min	2.37	4.95	4.67	8.96	6.88	13.41	9.20	18.28
max	4.42	7.28	7.50	12.36	10.66	17.32	14.02	24.26
Range	2.05	2.33	2.83	3.40	3.78	3.91	4.82	5.98
St. Dev.	0.72	0.94	0.98	1.08	1.29	1.25	1.70	1.76

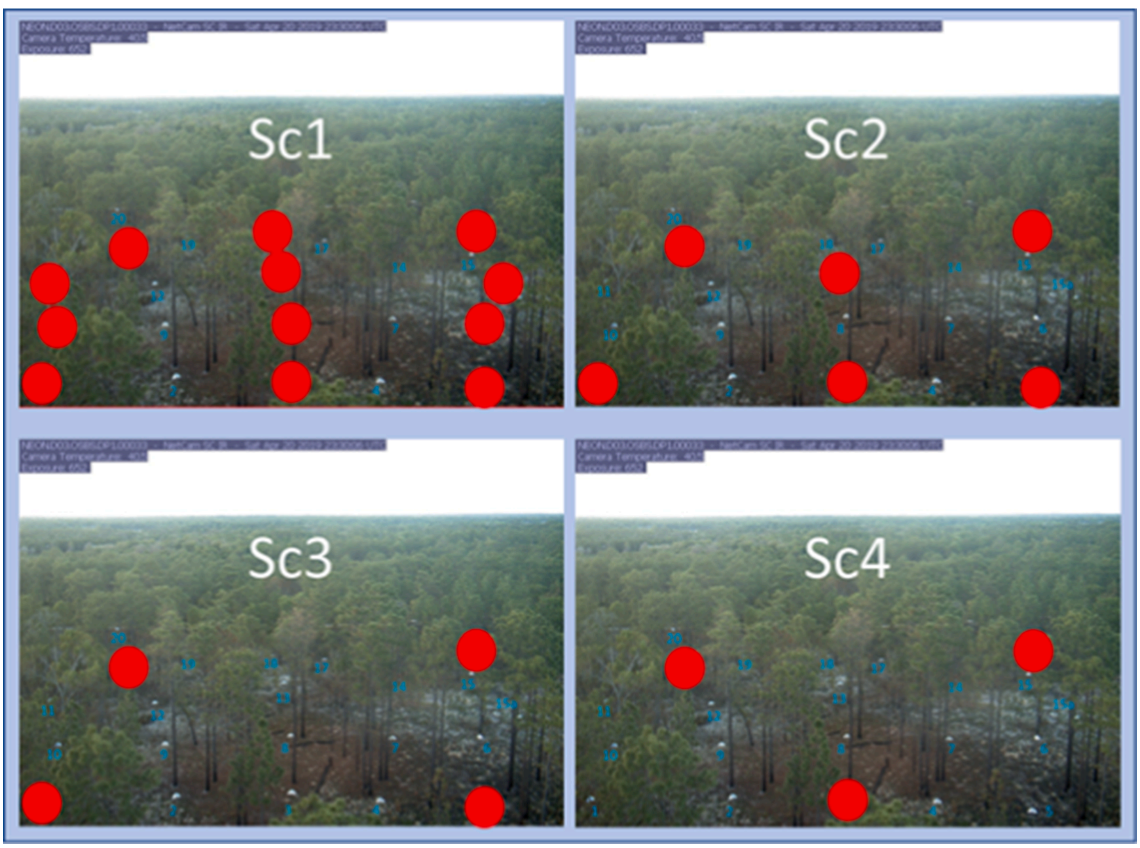

Fig. 9. Visual representation of the four GCPs scenarios.

image coordinates based on different options for the positional accuracy of the targets.

Table 8 shows the results of 1000 simulated space resection solutions and computation of the image coordinates of the checkpoints. Each simulation used GCP coordinates degraded with zero-mean random errors (σ_X=σ_Y= [0, 0.48, 0.98, 1.48, 1.98], σ_Z= $2\sigma_X$) to build the georeferencing model which was then used to compute the image coordinates of the checkpoints. Table 8 shows the standard deviations of the differences between the observed and computed image coordinates of the checkpoints for each degradation scale. It is observed that by doubling the degraded value, the mean of the standard deviations of d_x, and d_y (residuals from the truth) are almost doubled

4.3. Optimal number of targets

To make efficient use of the field survey time and resources without compromising accuracy, the optimal number of GCPs needed to georeference the PhenoCam imagery at OSBS was calculated. The optimal number of necessary GCPs depends on multiple factors and is often decided by the terrain of the site. Fig. 9 graphically illustrates four scenarios used for testing GCP configuration: Sc1, Sc2, Sc3, and Sc4, with each using a different number of GCPs: 12, 6, 4, and 3, respectively. Table 9 summarizes the residual 2D distance from the truth for each scenario. A set of example distances from image truth point to computed points for the validation are shown in Table 9, and the associated uncertainties of computed points are summarized in Table 10.

Table 9
Validation example distances from image truth point to computed coordinates (PhenoCam pixel units).

Check Point #	Residual 2D Distance (pixel)			
	Sc1	Sc2	Sc3	Sc4
2	1.46	1.54	2.26	2.54
4	1.42	1.61	2.20	2.18
7	1.26	1.13	1.89	2.43
9	0.72	0.81	1.32	0.81
12	1.71	1.52	2.20	0.65
14	0.80	0.39	0.86	1.39
15	1.17	1.46	0.88	0.98
17	0.87	0.47	1.07	0.97
19	2.36	1.93	2.39	1.82
20	2.30	2.33	3.06	1.27
Mean	1.41	1.32	1.81	1.50
Max	2.36	2.33	3.06	2.54
Min	0.72	0.39	0.86	0.65
Range	1.64	1.94	2.20	1.89
St. Dev.	0.58	0.62	0.74	0.69

Table 10
Validation example for propagated uncertainties for each computed coordinates of the truth points (PhenoCam pixel units).

Check Point #	Sc1		Sc2		Sc3		Sc4	
	σ_x	σ_y	σ_x	σ_y	σ_x	σ_y	σ_x	σ_y
2	0.72	0.78	1.00	0.79	0.86	0.93	1.21	0.78
4	0.71	0.81	0.50	0.67	0.88	0.99	1.04	0.79
7	0.44	0.56	0.37	0.52	0.61	0.77	0.70	0.64
9	0.45	0.57	0.70	0.66	0.60	0.75	0.85	0.65
12	0.45	0.55	0.54	0.60	0.62	0.73	0.59	0.58
14	0.50	0.59	0.39	0.50	0.62	0.73	0.41	0.49
15	0.69	0.69	0.52	0.59	0.82	0.85	0.53	0.56
17	0.47	0.64	0.37	0.48	0.57	0.73	0.32	0.42
19	0.59	0.69	0.48	0.55	0.75	0.81	0.41	0.49
20	0.99	0.93	0.74	0.71	1.21	1.06	0.66	0.72
Mean	0.60	0.68	0.56	0.61	0.75	0.84	0.67	0.61

4.4. Sensitivity analysis

After the convergence of the unified least squares solution, image coordinates of object space points may be computed. To understand the reliability of the resulting points, estimates of the precision corresponding to standard deviations of each computed coordinate were statistically derived. Fig. 10 illustrates the distribution of image-space positional uncertainty of each computed MODIS vertex using error ellipses formed by methods described in the Section titled “Error Ellipse”.

Semi-major and semi-minor axis values of the 95% confidence ellipsis are anticipated to be inversely proportional to the distance from the camera because the spatial resolution of oblique imagery decreases as the distance from the camera increases. In Fig. 11, the semi-major axis values for points are plotted against the distance from the camera to verify this is the case. Fig. 11 shows that the semi-axis value of the 95% confidence ellipsis is inversely proportional to the distance from the camera.

As per Table 11, the majority of uncertainty in the image space coordinates of the vertices can be explained by uncertainty in the estimated vertex position in object space.

4.5. Correlation among PhenoCam focal length and 3D coordinates

Another way high precision 3D position determination can potentially increase the use of obliquely mounted camera data is by helping to compensate for camera calibration deficiencies. An investigation of the correlation coefficients of the PhenoCam’s 3D coordinates and the focal length were run. The correlation matrix presented in Table 12 shows the correlations among PhenoCam’s focal length f and 3D coordinates (X_L, Y_L,Z_L). These results indicate a very weak positive (non-significant) correlation between f and X_L ($\rho_{fX_L=} = 0.07$), a very strong negative correlation between f and Y_L ($\rho_{fY_L} = -0.96$), and a moderate positive correlation between f and Z_L, thus, making it possible to compensate for camera calibration deficiency by having a high precision three-dimensional position for the camera.

5. Discussion

5.1. “Where” are PhenoCam pixels

A successful pixel-level georeferencing method for PhenoCam imagery is presented in this study. The robustness of the method is demonstrated through multiple tests of precision and accuracy and a test case using the NEON OSBS site.

Georeferencing helped answer the question of “where” which is without a doubt of utmost importance in studying phenological events. This work enables the geo-tagged PhenoCam pixels to be compared with other remote sensing datasets by associating pixels on the PhenoCam imagery with object space coordinates X, Y, and Z and indicates absolute location information indicating where it appears “in place” on the image with an accuracy of 1.5 PhenoCam pixels. Currently, there is no single method that could provide a tagging mechanism to geo-enable a phenological event automatically from PhenoCam observations, but this research has provided a critical step toward that goal. In this study, the canopy consisted of evergreen pines, so canopies were consistently leaf-on. Going forward, studies to automate or more finely capture phenological events than the 1.5 m pixel accuracy should include accounting for differences that may occur due to leaf-on and leaf-off differences for deciduous areas. Leaf-on versus leaf-off seasons could possibly be accommodated by using DTM vs DSM for denser deciduous vegetation.

5.2. Optimal number and quality of GCPs

An advantage to fixed position cameras is that the georeferencing process need only be carried out one time, using only GCPs. In this study, careful consideration of GCP factors contributed to successful implementation of the techniques. First, implementing an optimal number of GCPs is a valuable step to attain accurate results. It was investigated here by decreasing the number of GCPs until no significant difference remained among scenarios, which resulted in an optimal necessary number of GCPs of only three (see Fig. 9 and Table 7). In fact, three points provided reasonable accuracy similar to using 12 GCPs (Table 13). Second, the accuracy of GCPs in the study was carefully tracked because the quality of GCP coordinates has a direct impact on the quality of the computed results. In fact, uncertainty in surveyed GCPs translates to larger propagated errors in study results. Therefore, quantifying the uncertainties in GCP locations has implications in this study (Table 12), but should also be carried out in future studies at this and other sites, with careful regard to quality of GCP coordinates, which will determine the accuracy of the georeferencing.

5.3. Error ellipsis

It should be noted that the size of the 95% error ellipsis shown in Fig. 10 is represented in PhenoCam pixels, and PhenoCam pixel sizes (sample distances) increase along the view direction of the image toward the horizon; therefore, care should be taken with interpreting these uncertainty plots. Since sample distance increases along the view of the image, this can result in relatively similar sizes for all uncertainty ellipses when shown in ground units (such as meters) rather than PhenoCam pixels. In general, computing the semimajor and semiminor axis lengths of error ellipsis of computed image coordinates in meters instead of PhenoCam pixels will reflect more consistency in drawing the error ellipsis. Note that the converted meter values of σ_x, $\sigma_y$in Table 14 should not be confused by σ_{EAST}, σ_{NORTH}.

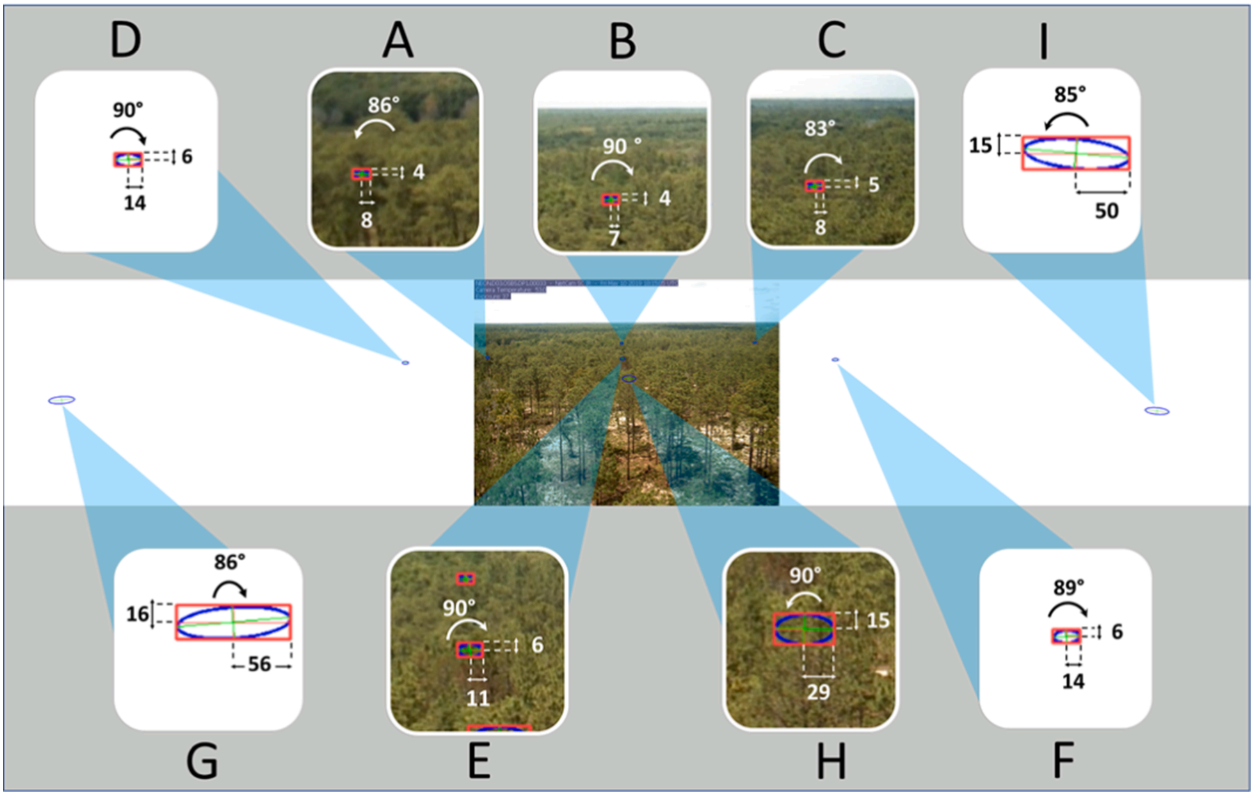

Fig. 10. Images and diagrams illustrating the error ellipses for each computed image coordinate pair corresponding to PhenoSynth/MODIS pixel/grid cell vertices. Vertices are labeled A-I and associated with the locations indicated. The red boxes represent 95% error rectangles, and the blue ellipsis represent 95% error ellipsis. The angular measurements represent clockwise rotation between the top part of y-axis and the major axis (in degrees), and the vertical and horizontal edge distances indicated in black or white text in PhenoCam pixel units represents the 2.45 $\sigma_x$horizontally and 2.45 $\sigma_y$vertically. (For interpretation of the references to colour in this figure legend, the reader is referred to the web version of this article.)

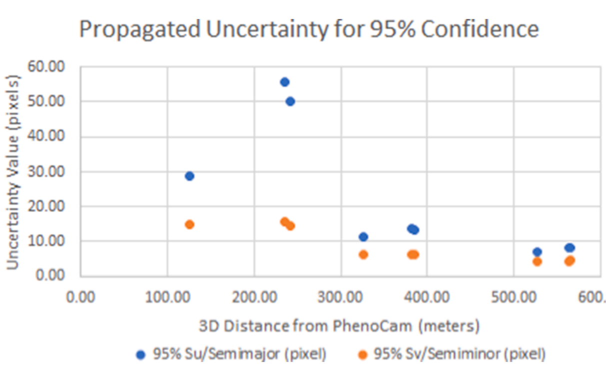

Fig. 11. shows distance vs. semi-major/minor axis.

5.4. Calibration

The main goal of this study was to provide an indication about the quality of the computed results without categorizing the sources propagated errors. From the sensitivity analysis results, it is evident that errors associated with lens distortion are absorbed and likely overpowered by higher-magnitude errors such as image mensuration and

Table 12
Correlation matrix for PenoCam's focal length f and EOPs (ω, φ, κ, X_L,Y_L,Z_L).

	f	X_L	Y_L	Z_L	ω	φ	K
f	1						
X_L	0.07	1					
Y_L	−0.96	−0.04	1				
Z_L	0.64	0.04	−0.65	1			
ω	−0.28	−0.05	0.22	−0.86	1		
φ	0.18	0.96	−0.15	0.11	−0.07	1	
K	−0.05	−0.46	0.04	−0.11	0.13	−0.33	1

Table 11
Sensitivity analysis input.

AOI Vertex	xi (pixel)	yi (pixel)	σ_{xi} (pixel)	σ_{yi} (pixel)	XO (m)	YO (m)	ZO (m)	σ_{XO} (m)	σ_{YO} (m)	σ_{ZO} (m)
A	47.49	706.56	1	1	403693.00	3285296.00	0.40	1	1	0.5
B	619.14	773.36	1	1	403894.00	3285295.00	21.10	1	1	0.5
C	1187.68	783.30	1	1	404095.00	3285293.00	22.27	1	1	0.5
D	−302.43	678.58	1	1	403691.00	3285096.00	14.81	1	1	0.5
E	623.82	707.16	1	1	403892.00	3285094.00	18.48	1	1	0.5
F	1530.59	713.16	1	1	404094.00	3285093.00	17.21	1	1	0.5
G	−1760.42	501.90	1	1	403689.00	3284896.00	24.27	1	1	0.5
H	652.03	620.45	1	1	403891.00	3284894.00	31.49	1	1	0.5
I	2880.44	509.32	1	1	404092.00	3284892.00	18.62	1	1	0.5

Table 13
Estimated focal length as well as the EOP Yl for each scenario.

Scenario	Focal Length	EOP Yl
Sc1	1473.86	3284769.78
Sc2	1474.27	3284769.72
Sc3	1473.55	3284769.79
Sc4	1465.06	3284770.56

Table 14
Rough conversion of PhenoCam's standard uncertainty pixel values to meters.

MODIS Vertex	Standard Uncertainty				Distance along optical axis (y-axis)
	From Pixels		To Meters		
	σ_x	σ_y	σ_x	σ_y	
A	3.30	1.77	1.18	0.63	526.27
B	2.91	1.78	1.04	0.63	525.27
C	3.31	1.85	1.17	0.66	523.27
D	5.67	2.55	1.25	0.56	326.27
E	4.58	2.47	1.01	0.54	324.27
F	5.53	2.54	1.21	0.56	323.27
G	22.74	6.59	1.95	0.56	126.20
H	11.73	6.09	0.99	0.51	124.27
I	20.44	6.30	1.69	0.52	122.27

GCP (Table 6). To quantify errors associated with lens distortion in the context of PhenoCam network cameras, there were several different factors to consider: (1) The challenge of capturing those parameters for all existing mounted cameras without disturbing data capture and georeferencing; (2) The sufficient reprojection accuracy that was achieved for PhenoCam imagery in this study while neglecting this error source; (3) Quantifying the overall uncertainties for each reprojected pixel/grid cell would reflect deviation caused by bending the ray of light as well as the displacement of the center of the lens. While quantifying this for the site at OSBS was considered, the determination of the relatively lower errors of associated lens distortion versus other error sources, this exercise was left to future studies with different objectives.

5.5. Computed image coordinates of MODIS pixels/grid cells

The projected surface in Fig. 10 indicates that none of the MODIS pixels/grid cells fall completely within the field of view of the camera, and that makes it difficult to correspond pixel-level MODIS products with georeferenced PhenoCam imagery. However, even partial representation of MODIS pixels will provide a suitable representation for cross-validation of satellite and ground data in many cases. This study provides a critical innovation in incorporating the geometric aspects of imaging, improving researchers' ability to understand the phenological phenomena captured with the camera, as well as enabling studies employing PhenoCam and MODIS data together.. In addition, this georeferencing method is concurrently being applied to remote sensing data with higher spatial resolution, such as Sentinel and Landsat, to be published in an upcoming manuscript. The results of the authors' other study and work of others who also apply the technique to various other remote sensing datasets have the potential to allow full reptesentation of data from satellite sources within the PhenoCam field of view and enable even more direct comparisons.

The results presented in this study illustrate that the techniques used are robust in overcoming the challenges associated with comparing measurements made at these disparate spatial scales. In fact, as seen in Fig. 12, by applying these techniques, a user can locate matching PhenoSynth pixels/grid cells with specific associated uncertainties, similar to the manner in which quality flags can be applied to PhenoSynth data to accommodate different research. This study provides an added benefit of flexibility in terms of validated levels of uncertainty, providing multiple analysis options when investigating levels of agreement. These factors increase the applicability of this technique because the requirements for spatial and temporal scales vary widely across disciplines, for example.

In this study, the derived geometery with quantified uncertainty enables better correspondence with MODIS data, a prime source of

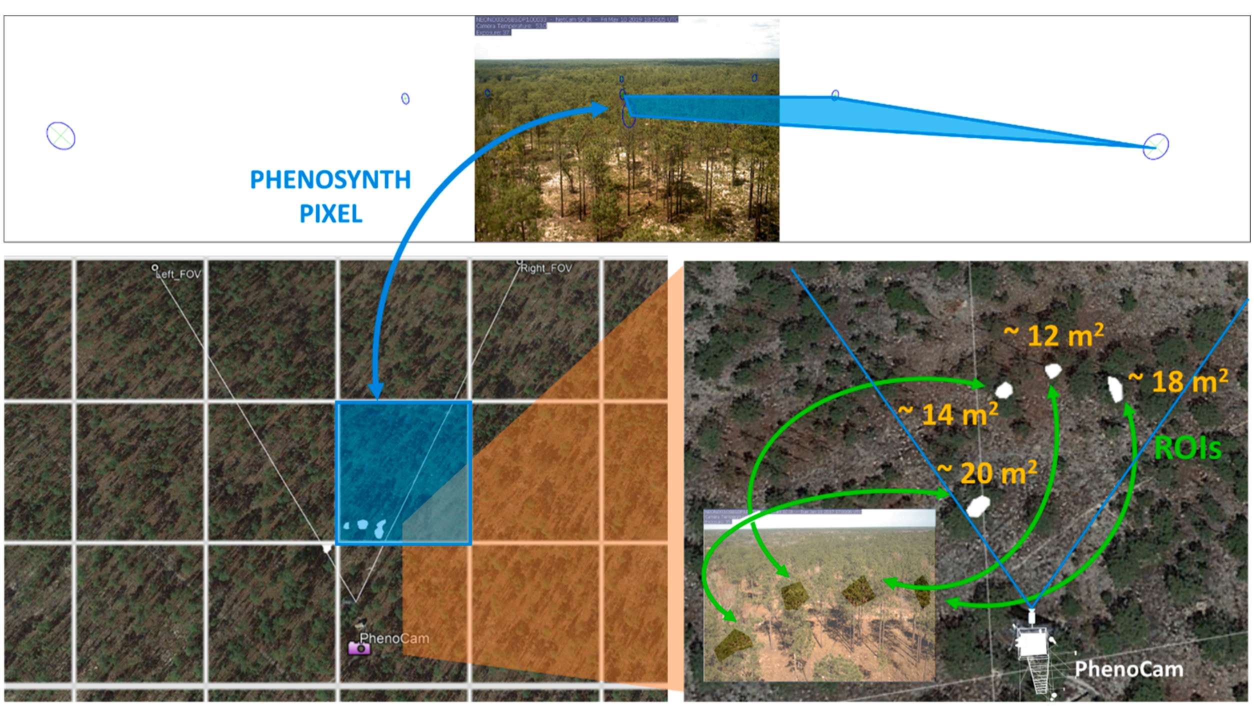

Fig. 12. Illustrative geometric and surface areas of MODIS vs. PhenoCam ROIs. Top: a PhenoCam image at OSBS with orientation estimation. Bottom-left: overhead view with corresponding MODIS pixel (blue box). Bottom-right: corresponding PhenoCam ROIs to the vegetation. (For interpretation of the references to colour in this figure legend, the reader is referred to the web version of this article.)

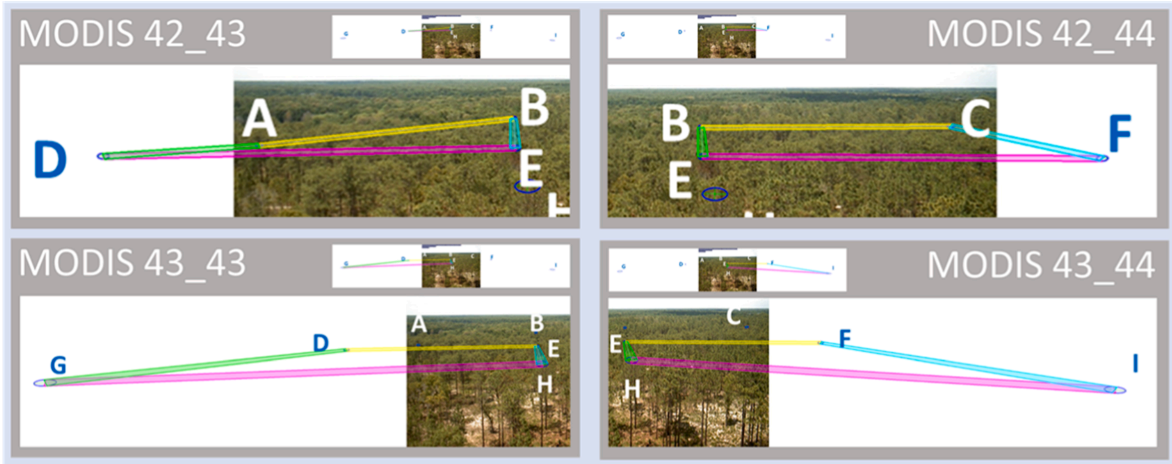

Fig. 13. Diagram of 95% confidence surfaces corresponding to each MODIS pixel/grid cell. Vertices are represented by A, B, C, D, E, F, G, H, I, and PhenoSynth pixel//grid cell IDs are represented by 42_43, 43_43, 42_44, 43_44. The inset in each panel is zoomed out to show the extent of all vertices' locations.

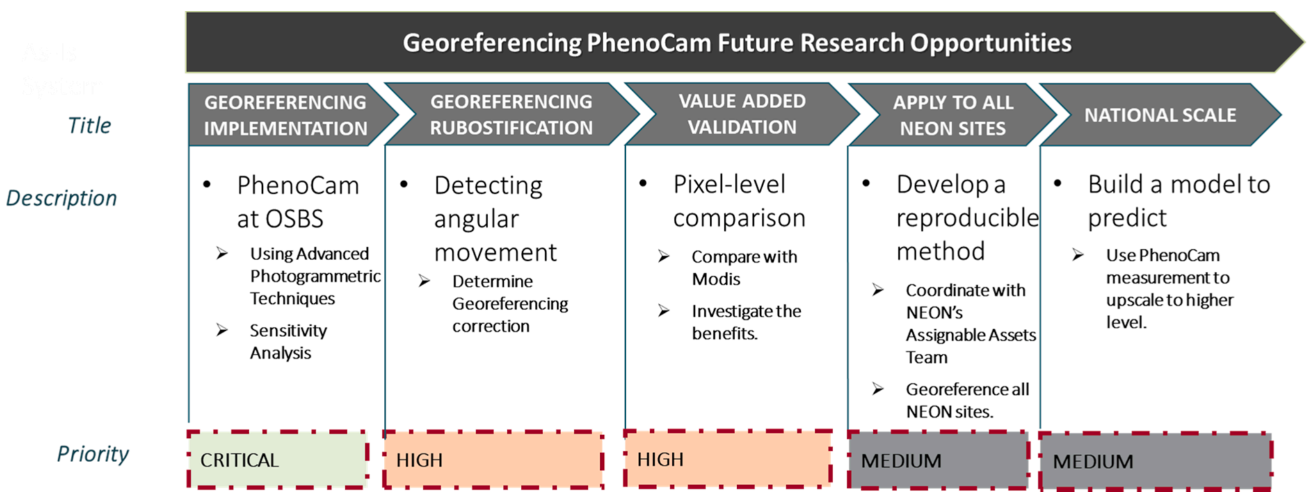

Fig. 14. Future research opportunities for Georeferencing PhenoCam from site to national scale implementation.

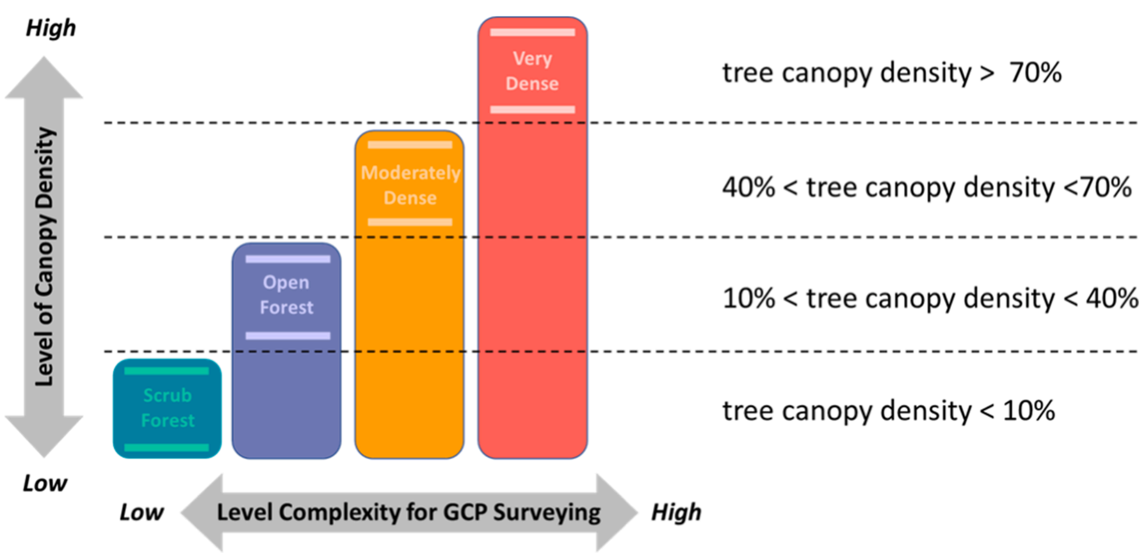

Fig. 15. Shows different complexity level for surveying GCPs within PhenoCam environments.

phenological analyes. Furthermore, based on this work, different geometries of the MODIS pixels/grid cells can be derived based on the necessity of vertices' uncertainties. For illustration of derived uncertainty and associated ellipse, Fig. 13 shows MODIS pixel/grid cell represented by 95% confidence interval. The higher the uncertainty of a certain vertex, the larger the overlap area between the corresponding neighboring MODIS pixels/grid cells. The results of this study open up multiple analysis options for researchers investigating the level of agreement by supplying a way to choose an acceptable uncertainty for the task and applying to their research.

5.6. Future work

The synergistic effect of georeferencing forms the basis of multiple research opportunities shown in Fig. 14, which can generally be divided into two categories: the work related to implementing, validating, and robustification of the georeferencing method; and the work related to implementing this at NEON sites and leverage it to build a prediction model at the national scale.

Of NEON's 47 terrestrial field sites across the United States where PhenoCams are mounted and based on the captured imagery of the field of view for each, they can be grouped into four broad types and subtypes (Fig. 15). OSBS falls under the group of a moderately dense canopy site. The differences in canopy cover density across sites will require careful planning to accurately plan and capture GCPs, an essential step to the georeferencing techniques. In locations of low-density cover, GCP location planning may be more straightforward and can be executed more easily, while in dense canopy cover, there may be few opportunities to collect GCPs from ground level, and alternative methods would be pursued. In general, it is recommended that for the next phases of implementation, several sites be chosen from low to moderate density cover to georeference PhenoCams.

6. Conclusion

In this work, usable area within PhenoCam imagery has been increased and precision from the relative location of ROI to an absolute location of all PhenoCam pixels was quantified. This work allowed fusion with MODIS data at known levels of uncertainty. The innovations presented in this study will allow for the fusion of the PhenoCam data with MODIS and many other currently available observations. Furthermore, the attention to detailed quantification of uncertainty helped reduce ambiguity, discrepancy, and disagreement and will serve future research in a similar way. Specifically, this effort has presented a practical approach for georeferencing terrestrial imagery, and it uses advanced photogrammetric techniques to provide phenological scientists a probability for any transformed coordinates from object space to image space coordinates with expected 95% confidence that the concerned feature is within an average of $\pm$ 22 PhenoCam pixels along x-axis and $\pm$ 9 PhenoCam pixels along y-axis PhenoCam pixels from its "computed" location (as shown in Table 4), and a corresponding object space standard deviation of less than 2 m. Furthermore, the statistical accuracy information is provided at the point-level, edge-level, and polygon-level, where geometrical properties of the satellite pixels/grid cells are represented in object space coordinates by the vertices and then associated with their corresponding image coordinates. By using lower input object space uncertainty at the centimeter level accuracy instead of meter level, and independent checkpoints to test image accuracy, this study confirmed that most of the computed image coordinates are on average distance of $\pm$ 1.5 PhenoCam pixels from the truth location. This level of detail enables other researchers to apply the techniques to meet the needs of their discipline. In ddition, these methods effectively address quality survey steps while providing straightforward, but flexible guidance for application in sites, especially those that are similar to OSBS. For instance, a minimum of three GCPs are shown to yield reasonable solutions similar to uncertainties resulting from surveying/measuring ($\pm$0.67 PhenoCam pixels along x-axis and $\pm$ 0.61 PhenoCam pixels along y-axis). Lastly, these methods allow the accurate computations of the camera EOPs and IOP by the use of photogrammetric steps.

One major novel aspect of this method is that, by precisely geolocating PhenoCam pixels, it becomes possible to tell a precise phenological story, not just from the PhenoCam pixel perspective, but from any related location's image data. PhenoCam pixels each tell a phenological story from flowering and leafing. Phenophases are constantly changing, and georeferencing these PhenoCam pixels can become a great tool to not only be able to witness that but precisely place it in context with history and other remotely sensed data. In summary, this approach empowers phenological scientists by determining accurate solutions and providing statistical information about the quality of that solution in a repeatable approach and with minimum difficulty.

Declaration of Competing Interest

The authors declare that they have no known competing financial interests or personal relationships that could have appeared to influence the work reported in this paper.

Acknowledgements

The National Ecological Observatory Network is a program sponsored by the National Science Foundation and operated under cooperative agreement by Battelle. This material is based in part upon work supported by the National Science Foundation through the NEON Program. Georeferencing PhenoCam imagery at Ordway Swisher Biological Station (OSBS) was supported by an OSBS Jumpstart grant from University of Florida Institute for Food and Agricultural Sciences (IFAS) to Benjamin Wilkinson. The authors gratefully acknowledge assistance offered by OSBS staff and manager, Andrew Rappe. We appreciate the support from the National Ecological Observatory Network (NEON), the onsite team, Felipe Sanchez, Satyra George, Ben Gottloeb, and Guy Fausnaught for their unlimited field support and head office team, specifically Megan Jones, Research Scientist, and Tristan Goulden, Remote Sensing Team Lead, especially for their insightful and timely responses to our meta-data needs. ADR acknowledges support from the National Science Foundation (EF-1702697).

Appendix A

Photogrammetric equations.

$$B^T = \begin{bmatrix}
\frac{\partial x_a}{\partial f} & \frac{\partial y_a}{\partial f} & \frac{\partial x_b}{\partial f} & \frac{\partial y_b}{\partial f} & \frac{\partial x_c}{\partial f} & \frac{\partial y_c}{\partial f} & \frac{\partial x_d}{\partial f} & \frac{\partial y_d}{\partial f} \\
\frac{\partial x_a}{\partial X_L} & \frac{\partial y_a}{\partial X_L} & \frac{\partial x_b}{\partial X_L} & \frac{\partial y_b}{\partial X_L} & \frac{\partial x_c}{\partial X_L} & \frac{\partial y_c}{\partial X_L} & \frac{\partial x_d}{\partial X_L} & \frac{\partial y_d}{\partial X_L} \\
\frac{\partial x_a}{\partial Y_L} & \frac{\partial y_a}{\partial Y_L} & \frac{\partial x_b}{\partial Y_L} & \frac{\partial y_b}{\partial Y_L} & \frac{\partial x_c}{\partial Y_L} & \frac{\partial y_c}{\partial Y_L} & \frac{\partial x_d}{\partial Y_L} & \frac{\partial y_d}{\partial Y_L} \\
\frac{\partial x_a}{\partial Z_L} & \frac{\partial y_a}{\partial Z_L} & \frac{\partial x_b}{\partial Z_L} & \frac{\partial y_b}{\partial Z_L} & \frac{\partial x_c}{\partial Z_L} & \frac{\partial y_c}{\partial Z_L} & \frac{\partial x_d}{\partial Z_L} & \frac{\partial y_d}{\partial Z_L} \\
\frac{\partial x_a}{\partial \omega} & \frac{\partial y_a}{\partial \omega} & \frac{\partial x_b}{\partial \omega} & \frac{\partial y_b}{\partial \omega} & \frac{\partial x_c}{\partial \omega} & \frac{\partial y_c}{\partial \omega} & \frac{\partial x_d}{\partial \omega} & \frac{\partial y_d}{\partial \omega} \\
\frac{\partial x_a}{\partial \phi} & \frac{\partial y_a}{\partial \phi} & \frac{\partial x_b}{\partial \phi} & \frac{\partial y_b}{\partial \phi} & \frac{\partial x_c}{\partial \phi} & \frac{\partial y_c}{\partial \phi} & \frac{\partial x_d}{\partial \phi} & \frac{\partial y_d}{\partial \phi} \\
\frac{\partial x_a}{\partial \kappa} & \frac{\partial y_a}{\partial \kappa} & \frac{\partial x_b}{\partial \kappa} & \frac{\partial y_b}{\partial \kappa} & \frac{\partial x_c}{\partial \kappa} & \frac{\partial y_c}{\partial \kappa} & \frac{\partial x_d}{\partial \kappa} & \frac{\partial y_d}{\partial \kappa} \\
\frac{\partial x_a}{\partial X_A} & \frac{\partial y_a}{\partial X_A} & \frac{\partial x_b}{\partial X_A} & \frac{\partial y_b}{\partial X_A} & \frac{\partial x_c}{\partial X_A} & \frac{\partial y_c}{\partial X_A} & \frac{\partial x_d}{\partial X_A} & \frac{\partial y_d}{\partial X_A} \\
\frac{\partial x_a}{\partial Y_A} & \frac{\partial y_a}{\partial Y_A} & \frac{\partial x_b}{\partial Y_A} & \frac{\partial y_b}{\partial Y_A} & \frac{\partial x_c}{\partial Y_A} & \frac{\partial y_c}{\partial Y_A} & \frac{\partial x_d}{\partial Y_A} & \frac{\partial y_d}{\partial Y_A} \\
\frac{\partial x_a}{\partial Z_A} & \frac{\partial y_a}{\partial Z_A} & \frac{\partial x_b}{\partial Z_A} & \frac{\partial y_b}{\partial Z_A} & \frac{\partial x_c}{\partial Z_A} & \frac{\partial y_c}{\partial Z_A} & \frac{\partial x_d}{\partial Z_A} & \frac{\partial y_d}{\partial Z_A} \\
\frac{\partial x_a}{\partial X_B} & \frac{\partial y_a}{\partial X_B} & \frac{\partial x_b}{\partial X_B} & \frac{\partial y_b}{\partial X_B} & \frac{\partial x_c}{\partial X_B} & \frac{\partial y_c}{\partial X_B} & \frac{\partial x_d}{\partial X_B} & \frac{\partial y_d}{\partial X_B} \\
\frac{\partial x_a}{\partial Y_B} & \frac{\partial y_a}{\partial Y_B} & \frac{\partial x_b}{\partial Y_B} & \frac{\partial y_b}{\partial Y_B} & \frac{\partial x_c}{\partial Y_B} & \frac{\partial y_c}{\partial Y_B} & \frac{\partial x_d}{\partial Y_B} & \frac{\partial y_d}{\partial Y_B} \\
\frac{\partial x_a}{\partial Z_B} & \frac{\partial y_a}{\partial Z_B} & \frac{\partial x_b}{\partial Z_B} & \frac{\partial y_b}{\partial Z_B} & \frac{\partial x_c}{\partial Z_B} & \frac{\partial y_c}{\partial Z_B} & \frac{\partial x_d}{\partial Z_B} & \frac{\partial y_d}{\partial Z_B} \\
\frac{\partial x_a}{\partial X_C} & \frac{\partial y_a}{\partial X_C} & \frac{\partial x_b}{\partial X_C} & \frac{\partial y_b}{\partial X_C} & \frac{\partial x_c}{\partial X_C} & \frac{\partial y_c}{\partial X_C} & \frac{\partial x_d}{\partial X_C} & \frac{\partial y_d}{\partial X_C} \\
\frac{\partial x_a}{\partial Y_C} & \frac{\partial y_a}{\partial Y_C} & \frac{\partial x_b}{\partial Y_C} & \frac{\partial y_b}{\partial Y_C} & \frac{\partial x_c}{\partial Y_C} & \frac{\partial y_c}{\partial Y_C} & \frac{\partial x_d}{\partial Y_C} & \frac{\partial y_d}{\partial Y_C} \\
\frac{\partial x_a}{\partial Z_C} & \frac{\partial y_a}{\partial Z_C} & \frac{\partial x_b}{\partial Z_C} & \frac{\partial y_b}{\partial Z_C} & \frac{\partial x_c}{\partial Z_C} & \frac{\partial y_c}{\partial Z_C} & \frac{\partial x_d}{\partial Z_C} & \frac{\partial y_d}{\partial Z_C} \\
\frac{\partial x_a}{\partial X_D} & \frac{\partial y_a}{\partial X_D} & \frac{\partial x_b}{\partial X_D} & \frac{\partial y_b}{\partial X_D} & \frac{\partial x_c}{\partial X_D} & \frac{\partial y_c}{\partial X_D} & \frac{\partial x_d}{\partial X_D} & \frac{\partial y_d}{\partial X_D} \\
\frac{\partial x_a}{\partial Y_D} & \frac{\partial y_a}{\partial Y_D} & \frac{\partial x_b}{\partial Y_D} & \frac{\partial y_b}{\partial Y_D} & \frac{\partial x_c}{\partial Y_D} & \frac{\partial y_c}{\partial Y_D} & \frac{\partial x_d}{\partial Y_D} & \frac{\partial y_d}{\partial Y_D} \\
\frac{\partial x_a}{\partial Z_D} & \frac{\partial y_a}{\partial Z_D} & \frac{\partial x_b}{\partial Z_D} & \frac{\partial y_b}{\partial Z_D} & \frac{\partial x_c}{\partial Z_D} & \frac{\partial y_c}{\partial Z_D} & \frac{\partial x_d}{\partial Z_D} & \frac{\partial y_d}{\partial Z_D}
\end{bmatrix} \tag{A-1}$$

$$W = \Sigma^{-1} = \begin{bmatrix}
\frac{1}{{\sigma_{X_a}}^2} & 0 & 0 & 0 & 0 & 0 & 0 & 0 \\
0 & \frac{1}{{\sigma_{Y_a}}^2} & 0 & 0 & 0 & 0 & 0 & 0 \\
0 & 0 & \frac{1}{{\sigma_{X_b}}^2} & 0 & 0 & 0 & 0 & 0 \\
0 & 0 & 0 & \frac{1}{{\sigma_{Y_b}}^2} & 0 & 0 & 0 & 0 \\
0 & 0 & 0 & 0 & \frac{1}{{\sigma_{X_c}}^2} & 0 & 0 & 0 \\
0 & 0 & 0 & 0 & 0 & \frac{1}{{\sigma_{Y_c}}^2} & 0 & 0 \\
0 & 0 & 0 & 0 & 0 & 0 & \frac{1}{{\sigma_{X_d}}^2} & 0 \\
0 & 0 & 0 & 0 & 0 & 0 & 0 & \frac{1}{{\sigma_{Y_d}}^2}
\end{bmatrix} \tag{A-2}$$

$$\Delta = \begin{bmatrix} df \\ dX_L \\ dY_L \\ dZ_L \\ d\omega \\ d\varphi \\ dk \\ dX_A \\ dY_A \\ dZ_A \\ dX_B \\ dY_B \\ dZ_B \\ dX_C \\ dY_C \\ dZ_C \\ dX_D \\ dY_D \\ dZ_D \end{bmatrix} \tag{A-3}$$

$$\varepsilon = \begin{bmatrix} X_a^m - X_a^c \\ Y_a^m - Y_a^c \\ X_b^m - X_b^c \\ Y_b^m - Y_b^c \\ X_c^m - X_c^c \\ Y_c^m - Y_c^c \\ X_d^m - X_d^c \\ Y_d^m - Y_d^c \end{bmatrix} \tag{A-4}$$

$$C = \begin{bmatrix} f^{00} - f^0 \\ X_L^{00} - X_L^0 \\ Y_L^{00} - Y_L^0 \\ Z_L^{00} - Z_L^0 \\ \omega^{00} - \omega^0 \\ \varphi^{00} - \varphi^0 \\ k^{00} - k^0 \\ X_A^{00} - X_A^0 \\ Y_A^{00} - Y_A^0 \\ Z_A^{00} - Z_A^0 \\ X_B^{00} - X_B^0 \\ Y_B^{00} - Y_B^0 \\ Z_B^{00} - Z_B^0 \\ X_C^{00} - X_C^0 \\ Y_C^{00} - Y_C^0 \\ Z_C^{00} - Z_C^0 \\ X_D^{00} - X_D^0 \\ Y_D^{00} - Y_D^0 \\ Z_D^{00} - Z_D^0 \end{bmatrix} \tag{A-5}$$

$$\dot{W} = \dot{\Sigma}^{-1} = \begin{bmatrix}
\frac{1}{\sigma_{X_D}^2} & 0 & 0 & 0 & 0 & 0 & 0 & 0 & 0 & 0 & 0 & 0 & 0 & 0 & 0 & 0 & 0 & 0 & 0 \\
0 & \frac{1}{\sigma_{X_D}^2} & 0 & 0 & 0 & 0 & 0 & 0 & 0 & 0 & 0 & 0 & 0 & 0 & 0 & 0 & 0 & 0 & 0 \\
0 & 0 & \frac{1}{\sigma_{X_D}^2} & 0 & 0 & 0 & 0 & 0 & 0 & 0 & 0 & 0 & 0 & 0 & 0 & 0 & 0 & 0 & 0 \\
0 & 0 & 0 & \frac{1}{\sigma_{X_D}^2} & 0 & 0 & 0 & 0 & 0 & 0 & 0 & 0 & 0 & 0 & 0 & 0 & 0 & 0 & 0 \\
0 & 0 & 0 & 0 & \frac{1}{\sigma_{X_D}^2} & 0 & 0 & 0 & 0 & 0 & 0 & 0 & 0 & 0 & 0 & 0 & 0 & 0 & 0 \\
0 & 0 & 0 & 0 & 0 & \frac{1}{\sigma_{X_D}^2} & 0 & 0 & 0 & 0 & 0 & 0 & 0 & 0 & 0 & 0 & 0 & 0 & 0 \\
0 & 0 & 0 & 0 & 0 & 0 & \frac{1}{\sigma_{X_D}^2} & 0 & 0 & 0 & 0 & 0 & 0 & 0 & 0 & 0 & 0 & 0 & 0 \\
0 & 0 & 0 & 0 & 0 & 0 & 0 & \frac{1}{\sigma_{X_D}^2} & 0 & 0 & 0 & 0 & 0 & 0 & 0 & 0 & 0 & 0 & 0 \\
0 & 0 & 0 & 0 & 0 & 0 & 0 & 0 & \frac{1}{\sigma_{X_D}^2} & 0 & 0 & 0 & 0 & 0 & 0 & 0 & 0 & 0 & 0 \\
0 & 0 & 0 & 0 & 0 & 0 & 0 & 0 & 0 & \frac{1}{\sigma_{X_D}^2} & 0 & 0 & 0 & 0 & 0 & 0 & 0 & 0 & 0 \\
0 & 0 & 0 & 0 & 0 & 0 & 0 & 0 & 0 & 0 & \frac{1}{\sigma_{X_D}^2} & 0 & 0 & 0 & 0 & 0 & 0 & 0 & 0 \\
0 & 0 & 0 & 0 & 0 & 0 & 0 & 0 & 0 & 0 & 0 & \frac{1}{\sigma_{X_D}^2} & 0 & 0 & 0 & 0 & 0 & 0 & 0 \\
0 & 0 & 0 & 0 & 0 & 0 & 0 & 0 & 0 & 0 & 0 & 0 & \frac{1}{\sigma_{X_D}^2} & 0 & 0 & 0 & 0 & 0 & 0 \\
0 & 0 & 0 & 0 & 0 & 0 & 0 & 0 & 0 & 0 & 0 & 0 & 0 & \frac{1}{\sigma_{X_D}^2} & 0 & 0 & 0 & 0 & 0 \\
0 & 0 & 0 & 0 & 0 & 0 & 0 & 0 & 0 & 0 & 0 & 0 & 0 & 0 & \frac{1}{\sigma_{X_D}^2} & 0 & 0 & 0 & 0 \\
0 & 0 & 0 & 0 & 0 & 0 & 0 & 0 & 0 & 0 & 0 & 0 & 0 & 0 & 0 & \frac{1}{\sigma_{X_D}^2} & 0 & 0 & 0 \\
0 & 0 & 0 & 0 & 0 & 0 & 0 & 0 & 0 & 0 & 0 & 0 & 0 & 0 & 0 & 0 & \frac{1}{\sigma_{X_D}^2} & 0 & 0 \\
0 & 0 & 0 & 0 & 0 & 0 & 0 & 0 & 0 & 0 & 0 & 0 & 0 & 0 & 0 & 0 & 0 & \frac{1}{\sigma_{X_D}^2} & 0 \\
0 & 0 & 0 & 0 & 0 & 0 & 0 & 0 & 0 & 0 & 0 & 0 & 0 & 0 & 0 & 0 & 0 & 0 & \frac{1}{\sigma_{X_D}^2}
\end{bmatrix} \tag{A-6}$$

Appendix B

Input for error standard deviation

(See Table B1).

Table B1
Input for Camera Parameters.

Camera Parameters	**f (pixel)**			**σ_f**		
	1500			150		
	length (pixel)			**width (pixel)**		
	1296			960		
	XL (m)	**YL (m)**	**ZL (m)**	**σ_{XL}**	**σ_{YL}**	**σ_{ZL}**
	403885.7	3,284,771	51.455	1	1	2
	ω (°)	**φ (°)**	**κ (°)**	**σ_ω**	**σ_φ**	**σ_κ**
	50	−2	0	100	100	100

Table B2
Input for GCPs with error standard deviation 0.48 m.

Ground Control Points (0.48 m)	GCP #	xi (pixel)	yi (pixel)	σ_{xi}	σ_{yi}	XO (m)	YO (m)	ZO (m)	σ_{XO}	σ_{YO}	σ_{ZO}
	1	34	80	1	1	403858.8	3,284,836	18.53	0.5	0.5	1
	3	649	94	1	1	403888.8	3,284,836	16.96	0.5	0.5	1
	5	1084	51	1	1	403907.8	3,284,830	19.44	0.5	0.5	1
	6	1096	226	1	1	403915.0	3,284,851	19.48	0.5	0.5	1
	8	646	232	1	1	403889.0	3,284,854	19.02	0.5	0.5	1
	10	91	209	1	1	403856.3	3,284,853	16.97	0.5	0.5	1
	11	74	319	1	1	403847.8	3,284,875	19.08	0.5	0.5	1
	13	629	360	1	1	403887.8	3,284,882	19.46	0.5	0.5	1
	15a	1192	277	1	1	403923.4	3,284,860	18.89	0.5	0.5	1
	16	1093	432	1	1	403931.2	3,284,901	18.35	0.5	0.5	1
	19a	254	421	1	1	403853.6	3,284,906	19.88	0.5	0.5	1

Table B3
Input for GCPs with error standard deviation 0.98 m.

Ground Control Points (0.98 m)	GCP #	xi (pixel)	yi (pixel)	σ_{xi}	σ_{yi}	XO (m)	YO (m)	ZO (m)	σ_{XO}	σ_{YO}	σ_{ZO}
	1	34	80	1	1	403858.6	3,284,838	19.25	1	1	2
	3	649	94	1	1	403888.3	3,284,836	18.07	1	1	2
	5	1084	51	1	1	403907.0	3,284,830	20.53	1	1	2
	6	1096	226	1	1	403915.1	3,284,850	21.48	1	1	2
	8	646	232	1	1	403889.7	3,284,853	18.32	1	1	2
	10	91	209	1	1	403856.2	3,284,852	15.99	1	1	2
	11	74	319	1	1	403848.3	3,284,875	17.02	1	1	2
	13	629	360	1	1	403889.9	3,284,882	19.30	1	1	2
	15a	1192	277	1	1	403923.9	3,284,859	21.90	1	1	2
	16	1093	432	1	1	403932.9	3,284,900	21.94	1	1	2
	19a	254	421	1	1	403855.8	3,284,905	18.43	1	1	2

Table B4
Input for GCPs with error standard deviation 1.48 m.

Ground Control Points (1.48 m)	GCP #	xi (pixel)	yi (pixel)	σ_{xi}	σ_{yi}	XO (m)	YO (m)	ZO (m)	σ_{XO}	σ_{YO}	σ_{ZO}
	1	34	80	1	1	403860.1	3,284,835	17.24	1.5	1.5	3
	3	649	94	1	1	403885.9	3,284,836	24.49	1.5	1.5	3
	5	1084	51	1	1	403905.3	3,284,831	20.05	1.5	1.5	3
	6	1096	226	1	1	403913.5	3,284,853	23.76	1.5	1.5	3
	8	646	232	1	1	403889.4	3,284,854	22.48	1.5	1.5	3
	10	91	209	1	1	403853.8	3,284,854	14.43	1.5	1.5	3
	11	74	319	1	1	403845.9	3,284,877	25.00	1.5	1.5	3
	13	629	360	1	1	403889.5	3,284,883	21.98	1.5	1.5	3
	15a	1192	277	1	1	403924.1	3,284,861	21.38	1.5	1.5	3
	16	1093	432	1	1	403933.5	3,284,903	20.65	1.5	1.5	3
	19a	254	421	1	1	403852.0	3,284,906	15.31	1.5	1.5	3

Table B5
Input for GCPs with error standard deviation 1.98 m.

Ground Control Points (1.98 m)	GCP #	xi (pixel)	yi (pixel)	σ_{xi}	σ_{yi}	XO (m)	YO (m)	ZO (m)	σ_{XO}	σ_{YO}	σ_{ZO}
	1	34	80	1	1	403861.5	3,284,833	16.66	2	2	4
	3	649	94	1	1	403886.8	3,284,838	18.24	2	2	4
	5	1084	51	1	1	403906.3	3,284,827	15.27	2	2	4
	6	1096	226	1	1	403914.4	3,284,853	26.22	2	2	4
	8	646	232	1	1	403892.6	3,284,856	22.21	2	2	4
	10	91	209	1	1	403857.7	3,284,852	16.16	2	2	4
	11	74	319	1	1	403845.2	3,284,872	16.82	2	2	4
	13	629	360	1	1	403887.3	3,284,880	22.61	2	2	4
	15a	1192	277	1	1	403920.3	3,284,859	19.77	2	2	4
	16	1093	432	1	1	403935.6	3,284,902	16.53	2	2	4
	19a	254	421	1	1	403854.3	3,284,902	23.23	2	2	4

Appendix C

Additonal information

Robustification effort

EOPs may change slightly when there is a moderate physical movement of the camera from, for example, wind resulting in moderate angular changes. These moderate deviations in the EOPs do not significantly affect the workflow in this study; however, future applications of these methods could benefit from accounting for greater degrees of physical movement associated with disturbances by, for example, an operator repositioning the camera or natural events such as storms or earthquakes. This topic will be addressed in a future study. Space resection observations are the image and object-space coordinates of several well-distributed control points.

Calibration effort

For practical implementation, we assume that the principal point (Wolf et al., 2014) coincides with the center of the image as it cannot be derived from the adjustment since it is correlated with the camera position. Similarly, we assumed that lens distortion parameters are negligible in the context of the application and expected accuracy, which was verified both by the PhenoCam team and by independent experiments in resolving them. We expecte this to be the case for all PhenoCams since they all use similar hardware, where most cameras use the same 6.2 mm lens (used for this case study). In general, lens design is constantly evolving and changing, and users do not have control over that. Resolving the complete set of IOPs including the lens distortion parameters precisely would require either removing the camera for laboratory calibration or by placing a calibration target closely in front of the tower-mounted camera. Both options are undesirable. We recommend, however, that future installation procedures include preliminary laboratory lens calibration to further investigate parameter significance and as a component of quality control.

References

Andriolo, U., Sanchez-Garcia, E., Taborda, R., 2019. Operational use of surfcam online streaming images for coastal morphodynamic studies. Remote Sensing 11 (1). https://doi.org/10.3390/rs11010078.

Battelle. (2020). Types of NEON Field Sites. Retrieved from https://www.neonscience.org/about-neon-field-sites/types-neon-field-sites.

Burt, J., Barber, G., Rigby, D., 2009. Elementary Statistics for Geographers (Third, Edition ed. Guilford Press, New York.

CloudCompare. (2020). GPL software. (version 2.11.3) Retrieved from http://www.cloudcompare.org/.

Conlin, M.P., Adams, P.N., Wilkinson, B., Dusek, G., Palmsten, M.L., Brown, J.A., 2020. SurfRCaT: A tool for remote calibration of pre-existing coastal cameras to enable their use as quantitative coastal monitoring tools. Softwarex 12, 100584. https://doi.org/10.1016/j.softx.2020.100584.

Crowson, R., Birkemeier, W., Klein, H., & Miller, H. (1988). SuperDuck NearShore Processes Experiment: Summary of Studies. Retrieved from.

Eckl, M.C., Snay, R.A., Soler, T., Cline, M.W., Mader, G.L., 2001. Accuracy of GPS-derived relative positions as a function of interstation distance and observing-session duration. J. Geod. 75 (12), 633–640. https://doi.org/10.1007/s001900100204.

Gerald, C. (1987). Two-Dimensional Measures of Accuracy in Navigational Systems. U.S Department of Transportation. Retrieved from https://rosap.ntl.bts.gov/view/dot/9683.

Ghilani, C. (2017). Adjustment Computations: Spatial Data Analysis. New York, John Wiley & Sons. Sixth Edition. Retrieved from https://doi.org/10.1002/9781119390664.ch19.

Holland, K. T., & Holman, R. A. (1997b). Video estimation of foreshore topography using trinocular stereo. Journal of Coastal Research, 13(1), 81-87. Retrieved from <Go to ISI>://WOS:A1997WL79900011.

Holland, K.T., Holman, R.A., Lippmann, T.C., Stanley, J., Plant, N., 1997a. Practical use of video imagery in nearshore oceanographic field studies. IEEE J. Oceanic Eng. 22 (1), 81–92. https://doi.org/10.1109/48.557542.

Holman, R., Sallenger, A., Lippmann, T., Haines, J., 1993. The application of video image processing to the study of nearshore processes. Retrieved from Oceanography 6, 78–85.

Holman, R.A., Stanley, J., 2007. The history and technical capabilities of Argus. Coast. Eng. 54 (6–7), 477–491. https://doi.org/10.1016/j.coastaleng.2007.01.003.

Holman, R.A., Symonds, G., Thornton, E.B., Ranasinghe, R., 2006. Rip spacing and persistence on an embayed beach. J. Geophys. Res.-Oceans 111 (C1). https://doi.org/10.1029/2005jc002965.

Hufkens, K., Friedl, M., Sonnentag, O., Braswell, B.H., Milliman, T., Richardson, A.D., 2012. Linking near-surface and satellite remote sensing measurements of deciduous broadleaf forest phenology. Remote Sens. Environ. 117, 307–321. https://doi.org/10.1016/j.rse.2011.10.006.

Johnson, D.J., Magee, L., Pandit, K., Bourdon, J., Broadbent, E.N., Glenn, K., Kaddoura, Y., Machado, S., Nieves, J., Wilkinson, B.E., Almeyda Zambrano, A.M., Bohlman, S.A., 2021. Canopy tree density and species influence tree regeneration patterns and woody species diversity in a longleaf pine forest. For. Ecol. Manage. 490, 119082. https://doi.org/10.1016/j.foreco.2021.119082.

Mikhail, E., Ackermann, F., 1982. Observations and least squares. University Press of America.

Morisette, J.T., Duffy, K.A., Weltzin, J.F., Browning, D.M., Marsh, R.L., Friesz, A.M., Zachmann, L.J., Enns, K.D., Landau, V.A., Gerst, K.L., Crimmins, T.M., Jones, K.D., Chang, T., Miller, B.W., Maiersperger, T.K., Richardson, A.D., 2021. PS3: the pheno-synthesis software suite for integration and analysis of multi-scale, multi-platform phenological data. Ecol. Inf. 65, 101400.

Richardson, A. D. (2007a). Terrestrial Ecosystems and Global Change. Department of Organismic & Evolutionary Biology. Richardson Lab, Harvard University. Retrieved from https://richardsonlab.fas.harvard.edu/index.html.

Richardson, A.D., Hufkens, K., Milliman, T., Aubrecht, D.M., Chen, M., Gray, J.M., Johnston, M.R., Keenan, T.F., Klosterman, S.T., Kosmala, M., Melaas, E.K., Friedl, M.A., Frolking, S., 2018. Tracking vegetation phenology across diverse North American biomes using PhenoCam imagery. Sci. Data 5 (1). https://doi.org/10.1038/sdata.2018.28.

Richardson, A.D., Jenkins, J.P., Braswell, B.H., Hollinger, D.Y., Ollinger, S.V., Smith, M.L., 2007b. Use of digital webcam images to track spring green-up in a deciduous broadleaf forest. Oecologia 152 (2), 323–334. https://doi.org/10.1007/s00442-006-0657-z.

Sanchez-Garcia, E., Balaguer-Beser, A., Pardo-Pascual, J.E., 2017. C-Pro: a coastal projector monitoring system using terrestrial photogrammetry with a geometric horizon constraint. ISPRS J. Photogramm. Remote Sens. 128, 255–273. https://doi.org/10.1016/j.isprsjprs.2017.03.023.

Schwartz, M.D. (Ed.), 2013. Phenology: An Integrative Environmental Science. Springer Netherlands, Dordrecht.

Sonnentag, O., Hufkens, K., Teshera-Sterne, C., Young, A.M., Friedl, M., Braswell, B.H., Milliman, T., O'Keefe, J., Richardson, A.D., 2012. Digital repeat photography for phenological research in forest ecosystems. Agric. For. Meteorol. 152, 159–177. https://doi.org/10.1016/j.agrformet.2011.09.009.

Stilwell, D., Pilon, R.O., 1974. Directional spectra of surface-waves from photographs. J. Geophys. Res. 79 (9), 1277–1284. https://doi.org/10.1029/JC079i009p01277.

Stockdon, H.F., Holman, R.A., 2000. Estimation of wave phase speed and nearshore bathymetry from video imagery. J. Geophys. Res.-Oceans 105 (C9), 22015–22033. https://doi.org/10.1029/1999jc000124.

Wilkinson, B., Lassiter, H.A., Abd-Elrahman, A., Carthy, R.R., Ifju, P., Broadbent, E., Grimes, N., 2019. Geometric targets for UAS lidar. Remote Sensing 11 (24). https://doi.org/10.3390/rs11243019.

Wolf, P., Dewitt, B., & Wilkinson, B. (2014). Elements of Photogrammetry with Applications in GIS (Fourth Edition ed.): McGraw-Hill Education: New York, Chicago, San Francisco, Athens, London, Madrid, Mexico City, Milan, New Delhi, Singapore, Sydney, Toronto.